Earth and Planetary Science Letters 539 (2020) 116184

Contents lists available at ScienceDirect

Earth and Planetary Science Letters

www.elsevier.com/locate/epsl

Evidence for a regional warm bias in the Early Cretaceous TEX_{86} record

Sebastian Steinig [a,*,1], Wolf Dummann [b,2], Wonsun Park [a], Mojib Latif [a,c], Stephanie Kusch [b,d], Peter Hofmann [b], Sascha Flögel [a]

[a] GEOMAR Helmholtz Centre for Ocean Research Kiel, Wischhofstr. 1-3, 24148 Kiel, Germany
[b] Institute of Geology and Mineralogy, University of Cologne, Zülpicher Str. 49a, 50674 Cologne, Germany
[c] Cluster of Excellence "The Future Ocean", Kiel University, Christian-Albrechts-Platz 4, 24118 Kiel, Germany
[d] University of Cologne-Centre for Accelerator Mass Spectrometry, Bernhard-Feilchenfeld-Str. 11, 50969 Cologne, Germany

ARTICLE INFO

Article history:
Received 17 April 2019
Received in revised form 17 February 2020
Accepted 24 February 2020
Available online 30 March 2020
Editor: L. Robinson

Keywords:
Cretaceous
paleotemperature
TEX_{86}
GDGTs
climate modelling
OAE 1a

ABSTRACT

The Cretaceous Period (145-66 Ma) provides an opportunity to obtain insights into the adaptation of the climate system to increased atmospheric greenhouse gas concentrations. The organic paleothermometer TEX_{86} is one of the few proxies available for reconstructing quantitative estimates of upper ocean temperatures of this time period. Here we show that the sedimentary TEX_{86} signal in the Early Cretaceous North and South Atlantic shows systematic differences to other Cretaceous samples. In particular, the relative increase in the fractional abundances of the crenarchaeol isomer compared to crenarchaeol exhibits similarities with surface sediments from the modern Mediterranean and Red Sea. Dedicated climate model simulations suggest that the formation of warm and saline deep waters in the restricted North and South Atlantic may have influenced TEX_{86} export dynamics leading to a warm bias in reconstructed upper ocean temperatures. Applying a regional calibration from the modern Mediterranean and Red Sea to corresponding TEX_{86} data significantly improves the model-data fit for the Aptian Oceanic Anoxic Event 1a and the overall comparison with other temperature proxies for the Early Cretaceous. Our results demonstrate the need to consider regional and temporal changes of the TEX_{86}-temperature relation for the reconstruction of deep-time ocean temperatures.

1. Introduction

The Cretaceous Period between 145 and 66 Ma is commonly considered a predominantly warm and equable greenhouse climate (Barron, 1983; O'Brien et al., 2017) with elevated levels of atmospheric CO_2 caused by enhanced volcanic activity (Foster et al., 2017). In combination with the ongoing breakup of Pangea (Blakey, 2008) and the simultaneous emergence of young and restricted ocean basins (Fig. 1), this period experienced multiple phases of dys- to anoxic conditions in the water column and deposition of marine organic-rich sediments (Jenkyns, 2010). These so-called Oceanic Anoxic Events (OAEs) reveal valuable insights into the response of the climate system to changes in marine ecosystems and the global carbon cycle. OAE 1a in the early Aptian (~125 Ma) and OAE 2 at the Cenomanian–Turonian boundary (~94 Ma) are the two most pronounced events throughout the Cretaceous and are characterised by long-term maxima in surface temperatures (O'Brien et al., 2017).

Quantitative estimates of upper ocean temperatures are necessary for estimating the magnitude of these past climate variations and to better validate paleoclimate model simulations. Reduced abundances of planktonic foraminifera and increased sedimentary calcite dissolution during the Early Cretaceous limit the application of the classic oxygen-isotope $\delta^{18}O$ SST proxy (O'Brien et al., 2017). The additional lack of alkenone-based temperature estimates makes the organic paleothermometer TEX_{86} (TetraEther indeX of tetraethers consisting of 86 carbons; Schouten et al., 2002) one of the few available techniques to reconstruct Early Cretaceous marine temperatures. The TEX_{86} proxy is based on the observation that the relative cyclisation of isoprenoidal glycerol dialkyl glycerol tetraethers (isoGDGTs) in membrane lipids of marine archaea increases with temperature (Schouten et al., 2002). Correlation of the isoGDGT distribution in modern core-top sediments with ambient water temperatures allows the reconstruction of past seawater temperatures. A variety of calibrations exist to convert measured TEX_{86} ratios (see Section 2.2; Schouten et al., 2002) to upper ocean temperatures. These partly arise from uncertainties in the actual export depth of the TEX_{86} signal ranging from the surface (Kim

* Corresponding author.
E-mail address: sebastian.steinig@bristol.ac.uk (S. Steinig).
[1] Present address: School of Geographical Sciences, University of Bristol, UK.
[2] Present address: Institute of Geosciences, Goethe-University Frankfurt, Altenhöferallee 1, 60438 Frankfurt am Main, Germany.

https://doi.org/10.1016/j.epsl.2020.116184
0012-821X/

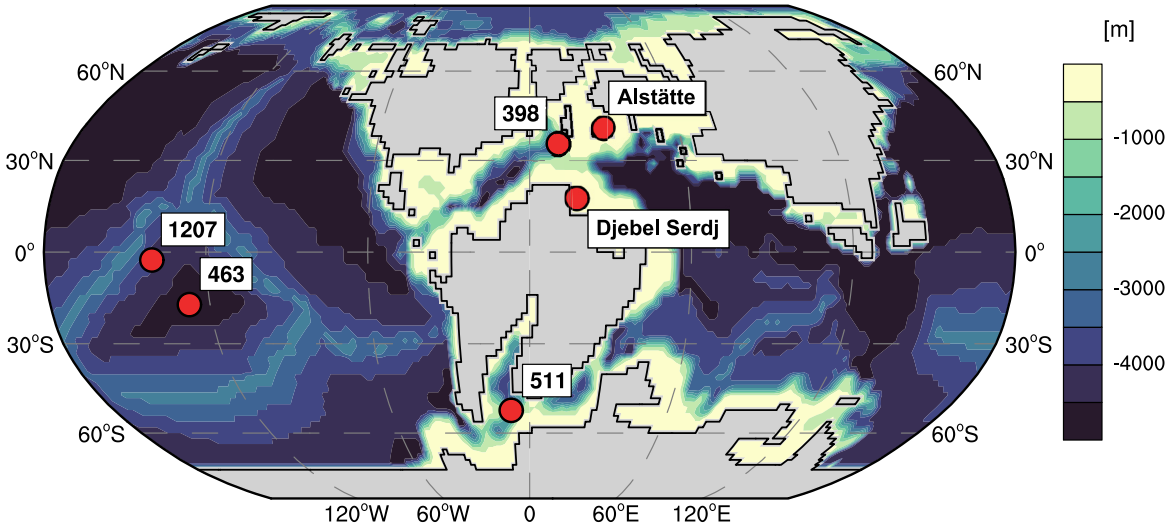

Fig. 1. Model bathymetry and study sites. Model geography and paleolocations (O'Brien et al., 2017) represent an early Aptian (~125 Ma) time slice. Contour interval is 500 m.

et al., 2010; Tierney and Tingley, 2014) down to 1000 m (Ho and Laepple, 2016). A recent comparison of the meridional gradients of ocean temperatures and core-top TEX_{86} values concludes that the global signal is most probably formed within the upper 200 m of the water column (Zhang and Liu, 2018).

Comparison of TEX_{86}-derived core-top temperatures with satellite measurements reveal systematic bias patterns of overestimated high-latitude and underestimated low-latitude temperatures (Tierney and Tingley, 2014). Specific areas known to have a TEX_{86}-SST relation different from the global open-ocean calibration are the modern Mediterranean (Kim et al., 2015) and Red Sea (Trommer et al., 2009). Surface sediments in these restricted basins show a strong increase in the fractional abundances of the crenarchaeol isomer and GDGT-2 with water depth for the upper 1000 m (Kim et al., 2015). The resulting warm bias in TEX_{86}^{H}-derived temperatures in deep-water sediments reaches up to 8 °C (Kim et al., 2015) and is also visible in the warm and saline Mediterranean Outflow Water along the Portuguese continental margin (Kim et al., 2016). Similar changes with water depth are observed for suspended particulate matter (SPM) samples from these regions (Kim et al., 2015, 2016) and imply an increased contribution of deep-dwelling Thaumarchaeota that have a different isoGDGT distribution (Taylor et al., 2013; Kim et al., 2015), possibly due to genetic controls (Villanueva et al., 2015; Kim et al., 2016). Paleorecords from the Mediterranean Sea indicate that the magnitude of this warm bias changed significantly through time and essentially vanished during the Last Glacial Maximum (Castañeda et al., 2010). Polik et al. (2018) also find temporal changes in the deviations of TEX_{86}- and alkenone-based SST estimates for different Pliocene-Pleistocene sapropel events and attribute this variability to the changing influence of different Thaumarchaeota populations with distinct isoGDGT distributions. A systematic offset between TEX_{86}^{H}-derived temperatures and other proxy methods has also been found for the Early Paleogene Southwest Pacific Ocean (Hollis et al., 2012) with an important influence of water depth on GDGT-2/GDGT-3 ratios (Taylor et al., 2013). As the overall TEX_{86}-predicted surface warming for the early Paleogene is consistent to other, independent proxy methods (Tierney et al., 2017; Hollis et al., 2019), this further highlights the potential importance of local environmental conditions for the interpretation of any recorded TEX_{86} signal.

Most of the Cretaceous TEX_{86} values, particularly those of the OAE 1a period, exceed the range of recorded present-day core-top data (Dumitrescu et al., 2006; Naafs and Pancost, 2016). In combination with the observed regional variability of TEX_{86} export dynamics, the applicability of modern global temperature calibrations for past greenhouse climates is questionable. To assess regional bias and calibration problems for the Cretaceous, we use a recently published quality-controlled compilation (O'Brien et al., 2017) and newly generated Cretaceous TEX_{86} data to identify systematic differences in the isoGDGT distributions. We compare TEX_{86}-derived SST and upper ocean temperatures from different calibrations with temperatures derived from a fully coupled atmosphere-ocean general circulation model, the Kiel Climate Model (Park et al., 2009). The model boundary conditions represent an early Aptian time slice to validate the internal consistency of the OAE 1a TEX_{86} record (Table 1), evaluate the local oceanographic setting for individual core locations and test the sensitivity of the results to the applied greenhouse gas forcing.

2. Methods

2.1. Model description

Climate model integrations were performed with the Kiel Climate Model (KCM, Park et al., 2009), a fully coupled atmosphere-ocean-sea ice general circulation model. The atmospheric component consists of the ECHAM5 spectral model (Roeckner et al., 2003) configured at a T42 horizontal resolution (~2.8° × 2.8°) with 19 vertical levels. The ocean-sea ice component NEMO uses a tripolar grid with a nominal horizontal resolution of 2° and 31 vertical levels (Madec, 2008). Existing model boundary conditions (Blöhdorn, 2013) represent an early Aptian (i.e. ~125 Ma) time slice based on global paleobathymetry reconstructions (Müller et al., 2008) complemented by information about shelf areas, coastlines and land topography (Blakey, 2008). Routing of river runoff to the ocean is calculated from the land orography (Hagemann and Dümenil, 1998). Simplified zonal mean vegetation properties were used for the land surface (Blöhdorn, 2013). No permanent land ice is assumed for the simulations, although seasonal snowfall and sea ice formation is permitted. Aptian-Albian CO_2 reconstructions based on stomatal indices of fossil conifers range from 500 to 1300 ppmv (Jing and Bainian, 2018). We therefore performed two integrations with 600 ($CRET_{600}$) and 1200 ($CRET_{1200}$) ppmv atmospheric CO_2 and a reduced solar constant of 1350 W/m^2. High resolution CO_2 reconstructions for OAE 1a (Naafs et al., 2016) average to ~1550 ppmv (carbon isotope segments C3-C6, n=19) and are therefore broadly consistent with $CRET_{1200}$. But Naafs et

Table 1
Overview of study sites. We combine new data from DSDP site 511 with published TEX_{86} data for the early Aptian OAE 1a (~125 Ma; see Section 2.5). Paleolatitude ranges derive from the spread in different reconstruction methods (see Supplementary Table S2).

Site	Reference	Location	Paleowater depth	Paleolatitude
DSDP 398	Naafs and Pancost (2016)	Proto-North Atlantic	500-2000 m[a,b]	22-36°N
DSDP 463	Schouten et al. (2003)	Mid-Pacific Mountains	~500 m[c]	7-35°S
DSDP 511	this study; Jenkyns et al. (2012)	Falkland Plateau	<750 m[a]	43-56°S
ODP 1207	Dumitrescu et al. (2006)	Shatsky Rise	~1300 m[d]	21°S-10°N
Alstätte 1 outcrop	Mutterlose et al. (2014)	Northwest Germany	< 200 m[e]	23°N-44°N
Djebel Serdj Formation	Naafs and Pancost (2016)	Tunisia	hemipelagic[f]	8°N-22°N

[a] Holbourn et al. (2001)
[b] Sibuet and Ryan (1979)
[c] Roth (1981)
[d] Bralower et al. (2002)
[e] Bottini and Mutterlose (2012)
[f] Heldt et al. (2008)

al. (2016) also show a stepwise increase of CO_2 levels throughout the event up to peak values between 1400 to 2800 ppmv. Therefore, parts of the TEX_{86} record at individual sites could reflect climatic signals generated at CO_2 concentrations significantly higher than in $CRET_{1200}$. As our model configuration develops a runaway greenhouse effect and becomes numerically unstable at CO_2 levels above 1200 ppmv, we extrapolate zonal mean temperatures for a further doubling of CO_2 concentrations to 2400 ppmv to generate a first-order approximation of simulated peak OAE 1a temperatures. We assume a linear climate sensitivity and define $CRET_{2400}$=$CRET_{1200}$+($CRET_{1200}$-$CRET_{600}$). Results for $CRET_{2400}$ are only used to identify TEX_{86} records incompatible with our model-predicted temperatures for the available OAE 1a CO_2 record. An additional simulation with pre-industrial levels of CO_2 ($CRET_{286}$) is performed to evaluate changes due to the different paleogeography and solar constant alone. Other greenhouse gases are held constant at their pre-industrial values due to a lack of available reconstructions. Experiment $CRET_{1200}$ was initialised with a homogeneous ocean temperature of 10 °C and salinity of 35 and integrated for 6000 model years. Experiments $CRET_{600}$ and $CRET_{286}$ were branched off from $CRET_{1200}$ at year 1000 and also integrated for an additional 5000 yr. The change in the globally depth-integrated ocean temperature for the last 1000 model years is below 0.15 °C for all experiments. All results are averaged over the last 500 yr of integration.

2.2. TEX_{86} paleothermometer

Pelagic Thaumarchaeota are considered the main source of biosynthesized isoGDGT lipids in marine environments. Different isoGDGT lipids are named according to their respective number of cyclopentane moieties, i.e. GDGT-0 through GDGT-3, with the exception of Crenarchaeol (Cren) and its isomer (Cren'), which contain 4 cyclopentane moieties and a cyclohexane ring. Highest correlation between different GDGT ratios and annual mean SST was initially reported for the TEX_{86} index (Schouten et al., 2002) defined as:

$$TEX_{86} = \frac{[GDGT-2]+[GDGT-3]+[Cren']}{[GDGT-1]+[GDGT-2]+[GDGT-3]+[Cren']} \quad (1)$$

To account for uncertainties in the actual export depth of the sedimentary TEX_{86} signal (Zhang and Liu, 2018) and differences in the extrapolation outside of the calibration range, we use several different methods to convert measured TEX_{86} values to upper ocean temperatures. The widely applied TEX_{86}^{H} (Kim et al., 2010) calibration uses a logarithmic relationship for an improved correlation with SSTs > 15 °C and is defined as:

$$SST = 68.4 \text{ x } TEX_{86}^{H} + 38.6 \quad (2)$$

with TEX_{86}^{H} = log(TEX_{86}). Similarly, a calibration of TEX_{86}^{H} with temperatures integrated over the upper 200 m of the water column was proposed (Kim et al., 2012) as:

$$T_{0-200m} = 54.7 \text{ x } TEX_{86}^{H} + 30.7 \quad (3)$$

A recent study (Ho and Laepple, 2016) suggests an even deeper TEX_{86} signal formation within the upper 1000 m of the water column. We calculate the respective proxy and model temperatures for the subsurface calibration ensemble with the "R" package "subcal" provided by the corresponding authors (Ho and Laepple, 2016). The assumption of a logarithmic relationship between surface temperature and TEX_{86} underlying TEX_{86}^{H} has been challenged over time as mesocosm experiments indicate a linear increase in GDGT cyclisation with temperature (Wuchter et al., 2004; Schouten et al., 2007). Resulting linear core-top calibrations lead to overall higher reconstructed temperatures for past greenhouse intervals (Tierney and Tingley, 2014; O'Brien et al., 2017). For comparison, we use a linear calibration that was specifically designed to reconstruct temperatures of warm Cretaceous settings by excluding present-day data from the Red Sea and regions with annual mean SSTs below 15 °C (O'Brien et al., 2017):

$$TEX_{86-linear} = 0.017 \text{ x } SST + 0.19 \quad (4)$$

2.3. New TEX_{86} measurements at DSDP 511 Falkland Plateau

We generated 69 new TEX_{86} samples from Deep-Sea Drilling Project site 511 to complement existing Early Cretaceous data from the same location (13 samples with available isoGDGT distributions, Jenkyns et al. 2012). Dried and ground sediments were successively extracted with methanol, dichloromethane:methanol (1:1, v:v), and dichloromethane using ultrasonication. The extracts were combined, dried under mild vacuum, and reacted with acid-activated copper clippings to remove elemental sulphur. The sulphur-free extracts were then partitioned over a self-packed silica column (deactivated with 1% ultrapure H_2O) using hexane, hexane:dichloromethane (2:1, v:v), and dichloromethane:methanol (1:1, v:v) successively. The final fraction containing the GDGTs was dissolved in a hexane:isopropanol mixture (95:5, v:v) and passed through a 0.45 mm polytetrafluoroethylene filter and C_{46} GDGT was added as internal standard. GDGTs were analysed using an Agilent 1290 UHPLC coupled to an Agilent 6460 QQQ mass spectrometer equipped with an APCI ion source. Published chromatographic conditions (Hopmans et al., 2016) were applied and the mass spectrometer was operated in selected ion monitoring mode (m/z 1302.4, 1300.4, 1298.4, 1296.4, 1292.4, 1050.1, 1048.1, 1046.1,

1036.1, 1034.1, 1032.1, 1022.1, 1020.1, 1018.1, 743.6). Resulting data is shown in Supplementary data set S1.

2.4. TEX_{86} compilations and GDGT screening

Besides our new measurements we use published compilations of present-day core-top (Tierney and Tingley, 2015) and Cretaceous (O'Brien et al., 2017) TEX_{86} samples. A particular advantage of the large Cretaceous compilation is the stringent application of several GDGT distribution parameters to screen for potential secondary, non-thermal effects on the TEX_{86} signal. The GDGT parameters and exclusion criteria used are the Branched and Isoprenoid Tetraether (BIT) Index > 0.3 (Hopmans et al., 2004), %GDGT-0 > 67% (Sinninghe Damsté et al., 2012), Methane Index (MI) > 0.5 (Zhang et al., 2011), $f_{Cren':Cren'+Cren}$ > 0.25 (O'Brien et al., 2017) and ΔRing Index |ΔRI| > 0.3 (Zhang et al., 2016).

150 samples from the Cretaceous compilation are excluded based on the above criteria (O'Brien et al., 2017). 80 out of the 105 data points from PAMA quarry are identified as potentially influenced by secondary processes and the rest of the data should be interpreted with caution (O'Brien et al., 2017). We therefore decided to exclude all samples from this site from the analysis. Similarly, about half of the available data from the Cismon core (Bottini et al., 2015) have been already excluded from the original Cretaceous compilation due to a potential influence of thermally mature organic matter input (Bottini et al., 2015; O'Brien et al., 2017). As nearly all remaining samples also have hopane 22S/(22S+22R) ratios > 0.1, indicating a potential bias towards colder reconstructed temperatures (Schouten et al., 2004), we excluded all Cismon samples from the analysis. [GDGT-0] is not provided for many samples from DSDP site 545. This by definition increases the fractional abundances of other individual isoGDGTs, but does not influence the ratios of multiple isoGDGTs discussed in this work (e.g. [Cren']/[Cren] or [GDGT-2]/[GDGT-3]). We therefore included all samples from DSDP site 545 in the analysis. We further include published Cenomanian–Turonian samples form the Kerguelen Plateau (Robinson et al., 2019) and OAE 1a samples from the Djebel Serdj Formation (Tunisia; Naafs and Pancost, 2016). Only one of the two samples from Djebel Serdj passed the described GDGT screening and is included in the OAE 1a temperature comparison, though we exclude it from the GDGT analysis due to a significant higher [GDGT-3] value than found in the rest of the Cretaceous data. Together with our new data from DSDP site 511 (n=69, all data points pass the GDGT screening described above), this results in 768 Cretaceous samples that provide individual isoGDGT distributions. We use two modern TEX_{86} core-top compilations as reference data. For comparability to the Cretaceous data, we only use samples from a global core-top data set (Tierney and Tingley, 2015) that provide individual isoGDGT distributions with an associated |ΔRI| < 0.3. Locations with an annual mean SST < 5 °C show an overall weak correlation with derived TEX_{86} ratios (Kim et al., 2008) and are therefore excluded from this analysis. The further removal of samples from the Mediterranean and Red Sea leads to 412 available present-day core top samples. A combined Mediterranean and Red Sea data set (n=195 with |ΔRI| < 0.3) is based on published compilations from the Mediterranean Sea (Kim et al., 2015) (n=172), the Red Sea (Trommer et al., 2009) (n=20, between 15-28°N) and three Red Sea samples from a global data set (Kim et al., 2008).

2.5. Age models and definition of OAE 1a

Absolute ages for all TEX_{86} samples were obtained from the published Cretaceous compilation (O'Brien et al., 2017) and are based on GTS2012 (Ogg et al., 2012). The isoGDGT analysis (see Fig. 5 and Fig. 6) is performed on all available samples passing the GDGT screening, while the model-proxy temperature comparison (see Fig. 2 and Fig. 7) is restricted to OAE 1a TEX_{86} samples. OAE 1a is defined as carbon isotope segments C3-C6 with corresponding depth intervals as reported in the original publications (Table 1). At DSDP site 511, the section between 540 and 516 mbsf has been interpreted as the local expression of OAE 1a (Jenkyns et al., 2012). A recent revision of biostratigraphic information, complemented by new carbon isotope data, however, put the presence of OAE 1a at DSDP Site 511 into question (Dummann et al., 2020). These new data indicate that the interval from 534.25 to 515 mbsf most likely comprises Early Aptian sediments of pre-OAE 1a age. As the average TEX_{86}^{H}-derived SST for OAE 1a (C3-C6) at DSDP site 398 is only about 1 °C higher than during pre-OAE 1a conditions (Naafs and Pancost, 2016), we include this interval at DSDP site 511 in our model-proxy comparison and interpret the associated temperatures as the lower end estimate of OAE 1a. The whole section from 553 to 481 mbsf (∼Neocomian to Aptian) is included in the isoGDGT comparison.

3. Results

3.1. OAE 1a ocean temperatures

The simulated global annual mean SST for the early Aptian with an atmospheric CO_2 of 1200 ppmv ($CRET_{1200}$) reaches 24.2 °C (Table 2), which is about 7 °C warmer than the pre-industrial reference simulation (PI_{286}). High-latitude warming is amplified and reduces the meridional temperature gradient between low and high latitudes from 25.3 °C in PI_{286} to 21.6 °C in $CRET_{1200}$. The Cretaceous continental configuration and the reduced solar constant in a simulation under pre-industrial CO_2 forcing ($CRET_{286}$) already reduce the temperature gradient by over 2 °C compared to PI_{286}. This change is even larger than the radiatively induced reduction by quadrupling atmospheric CO_2.

TEX_{86}-derived SSTs for OAE 1a (see Section 2.5 for a definition of OAE 1a) are higher than the simulated zonal mean temperatures in $CRET_{1200}$, both for the TEX_{86}^{H} (Fig. 2a, Eq. (2)) and the $TEX_{86-linear}$ calibrations (Fig. 2b). By definition, the $TEX_{86-linear}$ calibration yields a higher SST sensitivity at larger TEX_{86} values and mean SSTs above 40 °C for sites ODP 1207 and DSDP 398. Corresponding maximum TEX_{86}^{H}-derived temperatures are about 6 °C lower and in between $CRET_{1200}$ and $CRET_{2400}$ for the Pacific sites DSDP 463 and ODP 1207 and Djebel Serdj from Tunisia. Reconstructed SSTs for DSDP sites 511 and 398, as well as the Alstätte section from northwest Germany exceed the extrapolated $CRET_{2400}$ temperatures even for the logarithmic calibration (Fig. 2a). The overall misfit between model- and TEX_{86}-based temperatures decreases distinctly by applying a subsurface calibration (Fig. 2c-d). Shallow subsurface temperatures (integrated from 0-200 m, Eq. (3)) in the central equatorial Pacific at sites ODP 1207 and DSDP 463 range between 25-30 °C and agree with simulation $CRET_{1200}$. Temperatures from DSDP sites 511 (Falkland Plateau), 398 (North Atlantic) and Alstätte still exceed maximum simulated subsurface temperatures for OAE 1a. The mean offset to $CRET_{1200}$ varies between 4 °C for the North Atlantic and about 10 °C for the southern South Atlantic. Inclusion of the deeper subsurface (see Section 2.2) further reduces the simulated and reconstructed meridional temperature gradient and results in the overall best proxy agreement with $CRET_{1200}$ (Fig. 2d).

Fig. 3 illustrates a strong increase in the zonal differences in simulated low-latitude temperatures when comparing sea surface (Fig. 3a) and upper ocean temperatures (Fig. 3b). These enhanced longitudinal variations are caused by an increased influence of subsurface ocean dynamics on the otherwise radiatively controlled surface temperatures. The most pronounced features of zonal heterogeneity are the Western Pacific Warm Pool and eastern Pa-

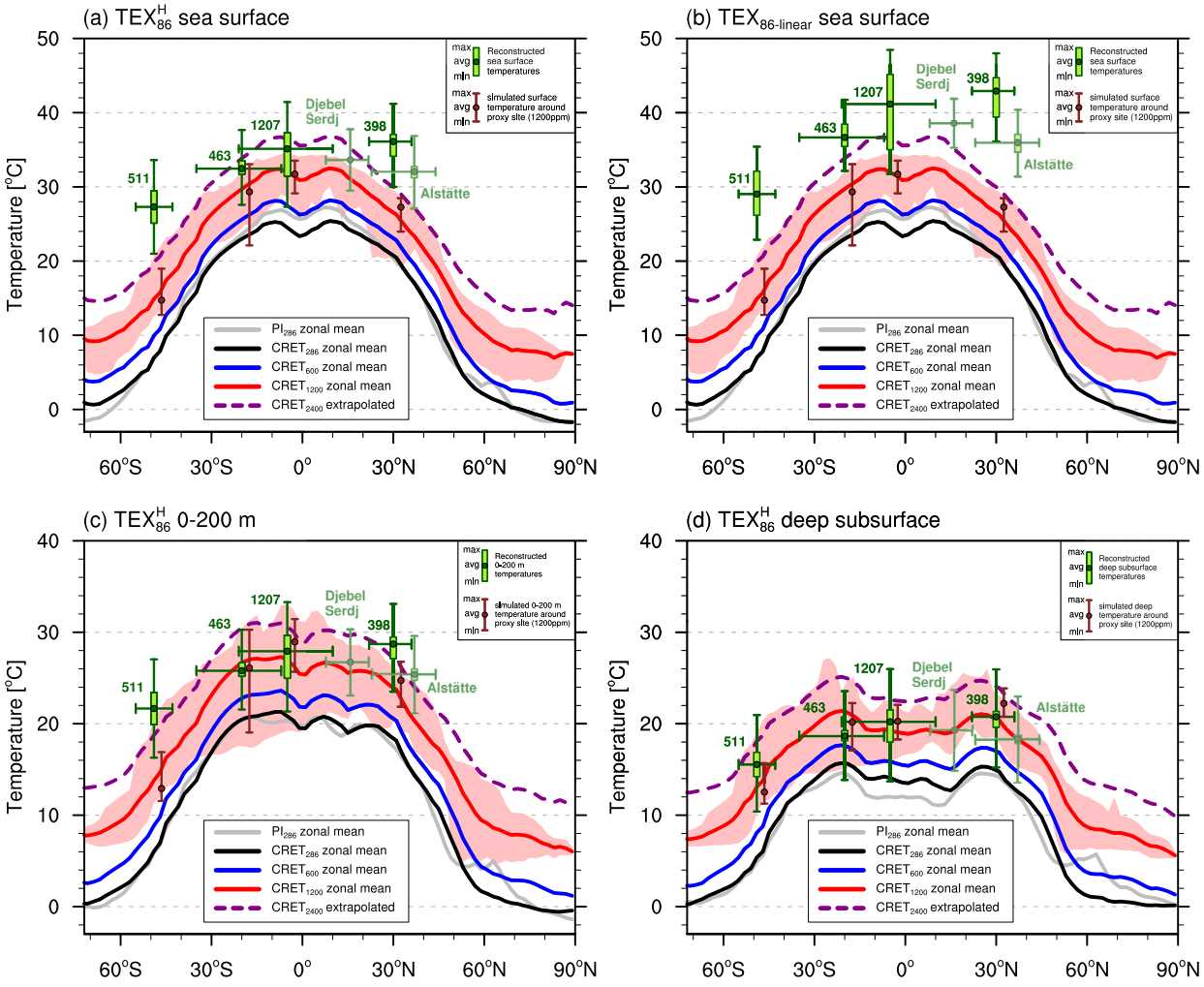

Fig. 2. Model-proxy comparison of upper ocean temperatures for OAE 1a. Calibrations used to convert TEX_{86} values to temperatures are (a) TEX^H_{86} SST (Eq. (2), Kim et al. 2010), (b) $TEX_{86-linear}$ SST (Eq. (4), O'Brien et al. 2017), (c) TEX^H_{86} 0-200 m depth-integrated (Eq. (3), Kim et al. 2012) and (d) a deep subsurface ensemble calibration (see Section 2.2, Ho and Laepple 2016). The two sites that were not included in the isoGDGT analysis are shown in lighter colour. Corresponding simulated annual mean ocean temperatures are zonally averaged and shown for (a-b) sea surface, (c) 0-200 m depth-integrated and (d) integrated over the deep subsurface (see Section 2.2). Shading represents the range of simulated temperatures at each latitude for experiment $CRET_{1200}$. Horizontal lines indicate the range of available paleolatitude estimates for each site (see Table 1). Vertical bars reflect the (green) 90% confidence interval for TEX_{86}-derived temperatures and the (red) range of simulated temperatures around the approximate paleolocation (uncertainty in latitude and ± 10° in longitude) for experiment $CRET_{1200}$. (For interpretation of the colours in the figure(s), the reader is referred to the web version of this article.)

Table 2
Simulated annual mean sea surface temperatures. Results are shown for the pre-industrial (PI) and Cretaceous (CRET) experiments and reported in °C. Subscripts indicate atmospheric CO_2 for the respective simulation.

Experiment	Global mean SST	Low-latitude SST $\lvert\phi\rvert$<30°	High-latitude SST $\lvert\phi\rvert$>60°	Meridional gradient $\lvert\phi\rvert$<30°-$\lvert\phi\rvert$>60°
PI_{286}	17.4	24.9	-0.4	25.3
$CRET_{286}$	17.1	23.5	0.4	23.1
$CRET_{600}$	19.8	26.2	3.2	23.0
$CRET_{1200}$	24.2	30.3	8.7	21.6

cific upwelling regions (Fig. 3c-d) caused by westward near-surface winds associated with the Pacific Walker Circulation. This east-west gradient makes the simulated temperatures at the respective core locations highly sensitive to the reconstructed paleoposition, especially with a stronger subsurface contribution to the TEX_{86} signal (Fig. 3d). In fact, the difference between the lowest and highest integrated temperature for the upper 200 m across the equatorial Pacific in $CRET_{1200}$ is up to 14 °C, nearly as large as the global meridional temperature gradient between low latitudes ($|\phi| < 30°$) and high latitudes ($|\phi| > 60°$) of 18 °C. In summary, TEX_{86}-based SST estimates for the North and South Atlantic exceed simulated temperatures even for peak CO_2 concentrations of 2400 pppmv. This is independent of the choice of a logarithmic or linear extrapolation and includes the consideration of the reported calibration uncertainties. TEX^H_{86}-derived temperatures in the Pacific Ocean are within the range of $CRET_{1200}$ and $CRET_{2400}$ due to the proximity to the West Pacific Warm Pool.

There are also clear differences in the ocean temperature profiles at individual study sites (Fig. 4a). While the central Pacific closely resembles the temperature profile of the global mean Cre-

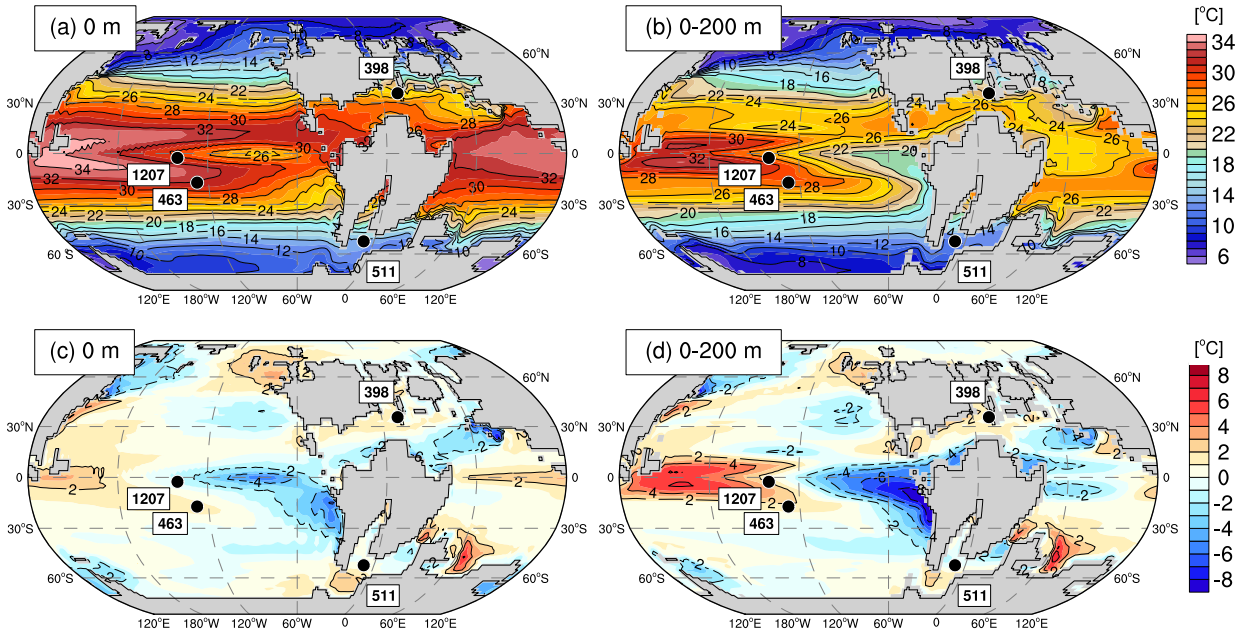

Fig. 3. Maps of simulated ocean temperatures. Temperatures are shown for experiment $Cret_{1200}$ for (a) the surface and (b) the upper 200 m, as well as their (c-d) deviations from the respective zonal mean value at each latitude. Values are in °C. Study sites are shown at their approximate early Aptian paleopositions (O'Brien et al., 2017).

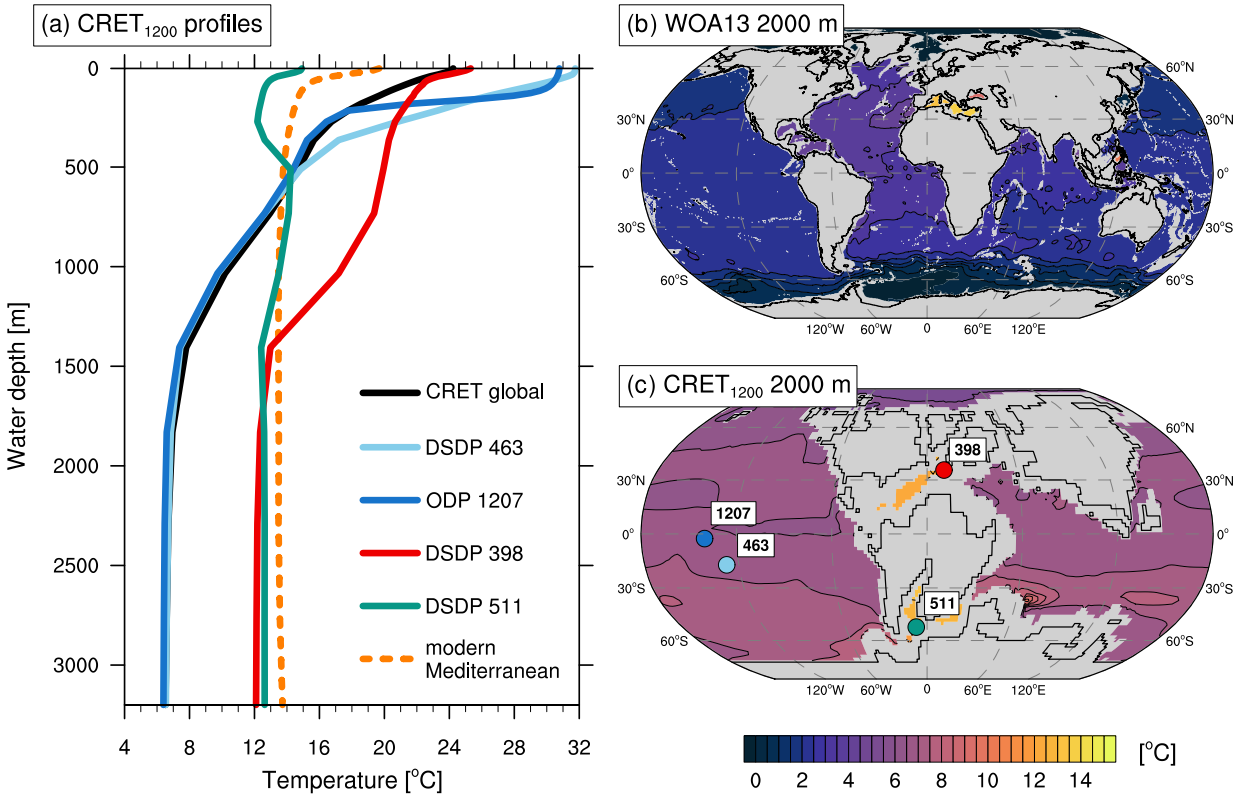

Fig. 4. Comparison of present-day and Cretaceous ocean temperatures. (a) Simulated and observed ocean profiles for annual mean temperature around study sites in $CRET_{1200}$ and the modern Mediterranean Sea, as well as maps of 2000 m ocean temperatures for (b) present day and (c) $Cret_{1200}$. Profiles are averaged over an area of ± 5° in longitude and latitude to account for uncertainty in paleolocation and model bathymetry. Therefore, water depths for the profiles represent maximum depth in the region used for averaging. Black contour line interval is 0.5 °C. Present-day data from the World Ocean Atlas 2013 (Locarnini et al., 2013).

taceous ocean, DSDP sites 398 and 511 are influenced by warmer waters at intermediate and deeper water depths. Simulated deep-water temperatures are about 6 °C warmer than the global mean and close to the 14 °C observed for the present-day Mediterranean Sea. The warm, saline deep waters result from excessive evaporation in low-latitude shallow shelf areas of the young North and South Atlantic (Fig. 1) and fill the deep, silled basins due to the lack of lateral deep-water exchange (Fig. 4c). This situation is comparable to the modern Mediterranean Sea where water mass exchange is severely limited by a shallow sill at ~300 m water depth near the narrow Strait of Gibraltar (Fig. 4b). While the depth ranges shown in Fig. 4b-c are not included in the discussed tem-

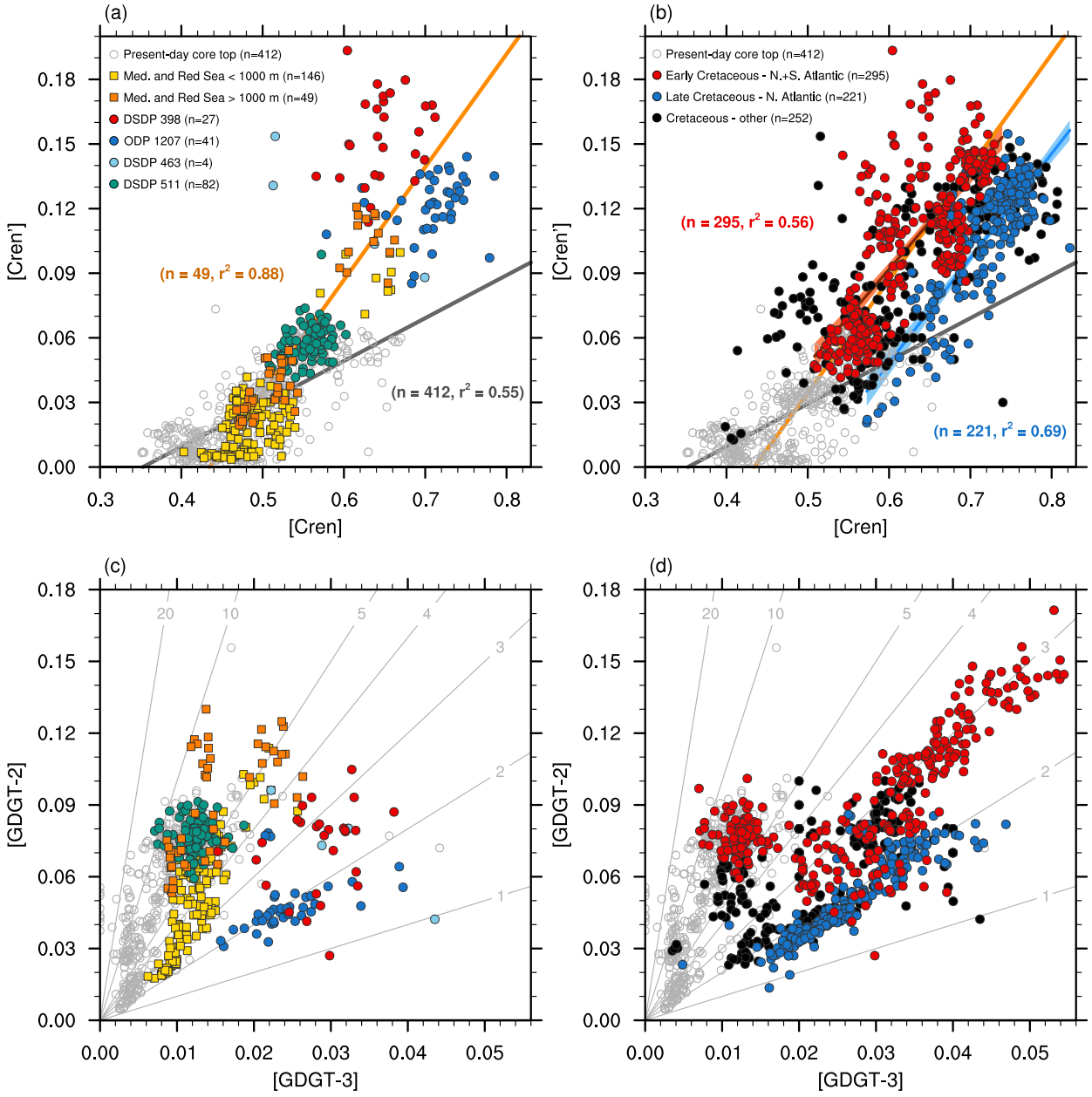

Fig. 5. Fractional abundances of isoGDGTs for modern and Cretaceous samples. Cross-plots are shown for fractional abundances of (a-b) the crenarchaeol isomer against crenarchaeol and (c-d) GDGT-2 against GDGT-3. Colours represent samples from (a,c) sites covering OAE 1a as well as from the present-day Mediterranean and Red Sea and (b,d) the complete Cretaceous compilation. Results for individual sites are shown in Supplementary Fig. S3 with respective references listed in Supplementary Table S1. Paleolocations of the Early Cretaceous North and South Atlantic sites (DSDP 603, DSDP 534, DSDP 398, ODP 1049, DSDP 545 and DSDP 511) and the Late Cretaceous North Atlantic sites (ODP 1258, ODP 1259, DSDP 367, Bass River, Meirs Farm, Brazos River and Shuqualak) are shown in Supplementary Fig. S1. Regression lines represent the simple linear regression for (grey) the global present-day and the (orange) combined Mediterranean and Red Sea core-top data for sites deeper than 1000 m. Linear regressions and their 95% confidence intervals are shown for the respective (red) Early Cretaceous North and South Atlantic and the (blue) Late Cretaceous North Atlantic groups. Lines in (c-d) represent contours of constant [GDGT-2]/[GDGT-3] ratios.

perature calibrations, the presence of warm and saline deep waters in the present-day restricted basins has been associated with an enhanced contribution of a deep water Thaumarchaeota population (Kim et al., 2015) with a distinct isoGDGT distribution (Trommer et al., 2009; Kim et al., 2016).

3.2. Comparison of Cretaceous and modern isoGDGT distribution patterns

Present-day core-top data (Fig. 5a) show a general increase in the fractional abundance of the crenarchaeol isomer ([Cren']) with increasing fractional abundances of crenarchaeol ([Cren]). An additional increase in [Cren'] abundances is visible for surface sediments from the Mediterranean and Red Sea with increasing water depth of the sample location. Cretaceous OAE 1a sites with high TEX_{86} values (>0.8) show fractional abundances of [Cren'] exceeding the range of present-day data (see Supplementary Fig. S2). Despite having similar TEX_{86} values, samples from DSDP site 398 are generally enriched in the proportion of [Cren'] and reduced in [Cren] compared to samples from ODP site 1207. Abundances for DSDP site 511 lie within the upper end of present-day [Cren']. Samples from the North Atlantic (398) and Falkland Plateau (511) match or exceed the regression of deeper sediments from the Mediterranean and Red Sea. Most of the ODP site 1207 samples show lower fractional abundances of [Cren'] than DSDP

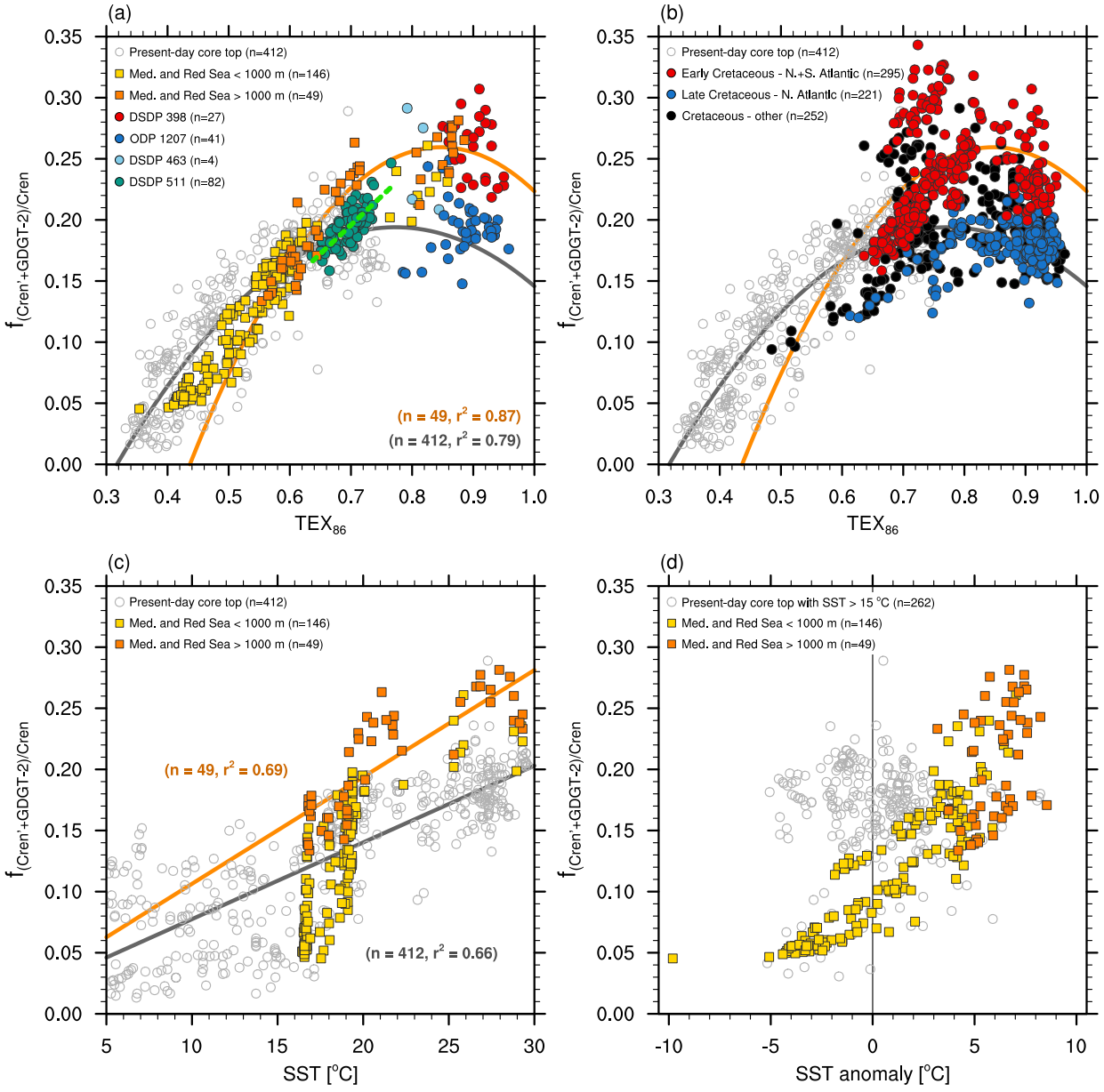

Fig. 6. New isoGDGT ratio compared to TEX_{86} and SST. Shown are cross-plots of the $f_{(Cren'+GDGT-2)/Cren}$ ratio (Eq. (5)) against (a-b) TEX_{86}, (c) satellite-derived annual mean SST and (d) the difference between TEX_{86}^{H}-derived and satellite-measured temperatures. As the TEX_{86}^{H} calibration should not be used to reconstruct temperatures below 15 °C (Kim et al., 2010) these samples are excluded in panel (d). Colours represent samples from (a) sites covering OAE 1a as well as from the present-day Mediterranean and Red Sea, (b) the whole Cretaceous compilation and (c-d) the present-day Mediterranean and Red Sea. Results for individual sites are shown in Supplementary Fig. S3 with respective references listed in Supplementary Table S1. Solid lines show (a-b) the quadratic polynomial and (c) linear regression for the present-day as well as the combined deep Mediterranean and Red Sea core-top data for sites deeper than 1000 m. The dashed line in (a) represents the linear regression for DSDP site 511 only.

site 398, but values for [Cren] and [Cren'] are still outside the present-day range. Despite the considerable spread in the data, the general tendency of a higher [Cren']/[Cren] ratio in samples from the restricted Early Cretaceous North and South Atlantic can also be seen in the rest of the Cretaceous data set (Fig. 5b) and especially in relation to samples from the Late Cretaceous North Atlantic. This systematic enrichment of [Cren'] might indicate a different temperature-isoGDGT relationship or an additional non-temperature influence on these samples that is not detected by the commonly applied GDGT screening criteria (see Section 2.4).

Ratios of the fractional abundances of GDGT-2 and GDGT-3 ([GDGT-2]/[GDGT-3]) in the Cretaceous are predominantly lower than for the modern core tops (Fig. 5d) due to a decrease in [GDGT-2] and an increase in [GDGT-3] at higher TEX_{86} values (>0.7, see Supplementary Fig. S2). Samples from the Atlantic Ocean show increased fractional abundances of [GDGT-2] during the Early Cretaceous compared to the Late Cretaceous. Again, DSDP sites 398 and 511 show overall higher [GDGT-2]/[GDGT-3] ratios than the respective samples from ODP site 1207. Ratios for the Falkland Plateau range between 4 to 12, similar to deeper sediments from the Mediterranean Sea.

The systematic differences in isoGDGT distributions can also be identified in relation to derived TEX_{86} ratios. We combine the previous results in the ratio of fractional abundances of [Cren'] and [GDGT-2] compared to [Cren] in eq. (5):

$$f_{(Cren'+GDGT-2)/Cren} = \frac{[Cren'] + [GDGT-2]}{[Cren] + [Cren'] + [GDGT-2]} \quad (5)$$

Values for $f_{(Cren'+GDGT-2)/Cren}$ show a strong increase with TEX_{86} for samples from DSDP sites 511 and 398 (Fig. 6a) and the

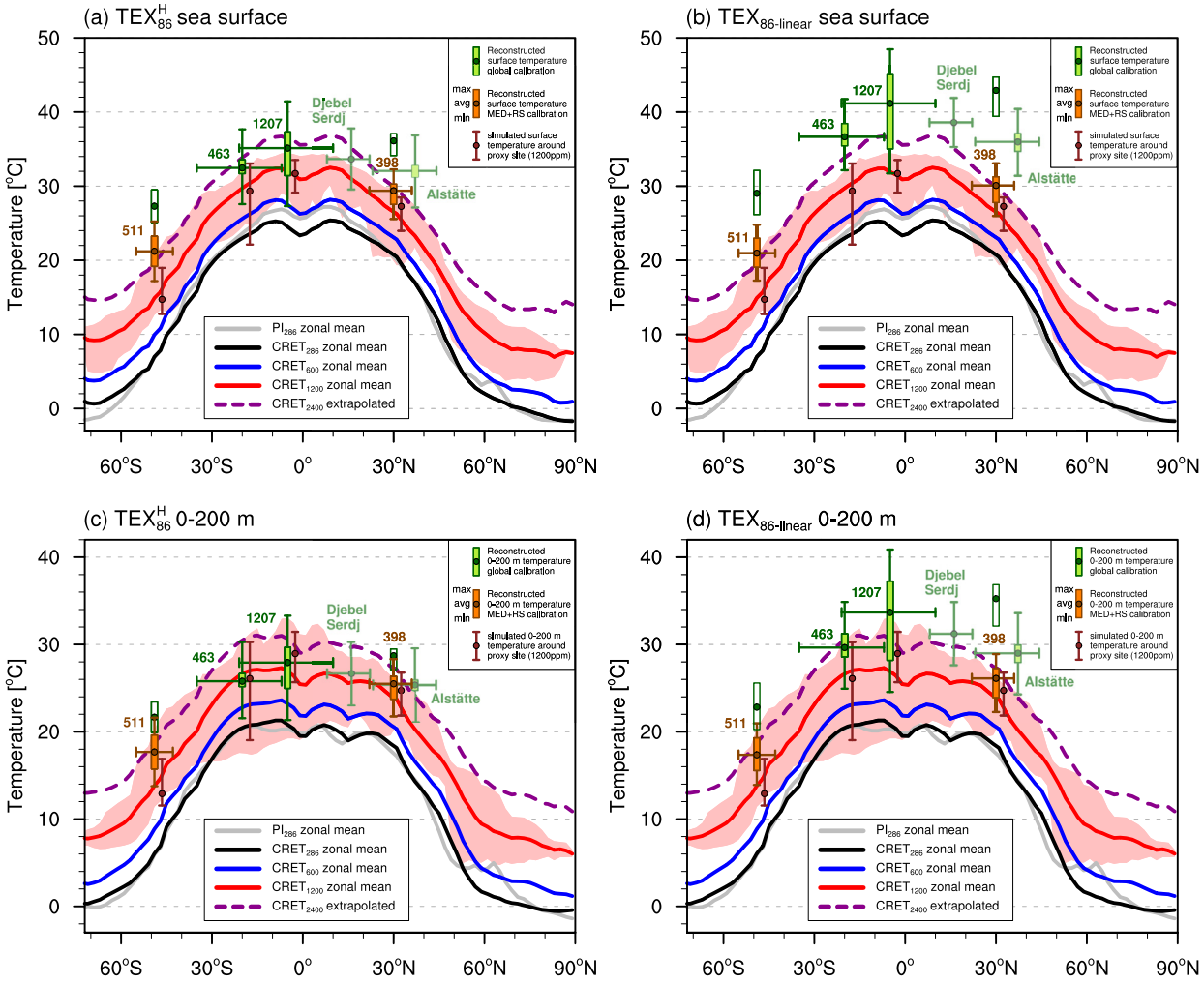

Fig. 7. Model-proxy comparison of upper ocean temperatures for OAE 1a. Similar to Fig. 2, but applying regionally different temperature calibrations for the TEX_{86} samples to reconstruct (a-b) SSTs and (c-d) 0-200 m subsurface temperatures. We use global calibrations for Sites 463 and 1207, i.e. Eq. (2) in (a), Eq. (4) in (b), Eq. (3) in (c) and a modified subsurface version of $TEX_{86-linear}$ (Eq. (6), Supplementary Fig. S7) in (d). Regional calibrations for Sites 511 and 398 are based on core-top samples form the Mediterranean and Red Sea following the approach of Kim et al. (2015) (Eq. (7)-(10) in Supplementary Fig. S8). The two sites that were not included in the isoGDGT analysis are shown in lighter colour with temperatures reconstructed by the respective global core-top calibrations.

rest of the Early Cretaceous North and South Atlantic (Fig. 6b) that follows or exceeds the deep Mediterranean and Red Sea regression. ODP site 1207 and most of the rest of the available Cretaceous data plot closely to the extrapolated global present-day core-top regression. As the majority of the Cretaceous samples, including DSDP sites 398, 463 and 1207, lie outside of the modern calibration range, any extrapolation of the present-day $f_{(Cren'+GDGT-2)/Cren}$ ratio will critically depend on the choice of the regression model. The quadratic polynomial shown in Fig. 6 is chosen based on its higher correlation coefficient (r^2=0.79) and less-structured residuals compared to a linear regression (see Supplementary Fig. S4). Irregardless of the applied regression model, the clear separation between the Early and Late Cretaceous Atlantic Ocean samples is a striking result.

Absolute values of $f_{(Cren'+GDGT-2)/Cren}$ for DSDP site 511 are comparable to sediments from the deep Mediterranean Sea, but both data sets are within the observed range of the global core-top data at the respective TEX_{86} range. Nevertheless, we note that the increase in $f_{(Cren'+GDGT-2)/Cren}$ with TEX_{86} for samples from site 511 (see dashed regression line in Fig. 6a and Supplementary Fig. S4) is stronger than in the global core-top data and resembles the higher $f_{(Cren'+GDGT-2)/Cren}$ sensitivity for samples from the deep Mediterranean Sea. Besides the expected increase in [Cren'] with temperature, these samples show an additional enrichment of [Cren'] with water depth that is not present in global core-top data (Kim et al. 2015 and Supplementary Fig. S5). The higher relative abundances of [Cren'] and [GDGT-2] lead to higher TEX_{86} values in deeper sediments (Kim et al., 2015), despite similar surface temperatures (Fig. 6c). As previously reported (Kim et al., 2015), the resulting warm bias for TEX^H_{86}-derived SSTs amounts to up to 8 °C and increases for higher $f_{(Cren'+GDGT-2)/Cren}$ ratios (Fig. 6d). The increasing deviations from the global $f_{(Cren'+GDGT-2)/Cren}$-TEX_{86} relation at higher TEX_{86} values in samples from DSDP site 511 and the Early Cretaceous North Atlantic might indicate a similar dominant control of [Cren'] and [GDGT-2] on the derived TEX_{86} values in these samples.

3.3. Implications for Early Cretaceous ocean temperatures

The previous two sections demonstrated that (i) the Early Cretaceous North and South Atlantic provided special oceanographic conditions due to the combination of the prevailing greenhouse climate and the paleogeographic restriction and (ii) that the isoGDGT abundances of TEX_{86} samples from these young ocean basins show systematic differences to other Cretaceous records. Based on these two lines of evidence, we hypothesise that the environmental conditions for the TEX_{86} signal formation in the young North and South Atlantic might have been more comparable to the situa-

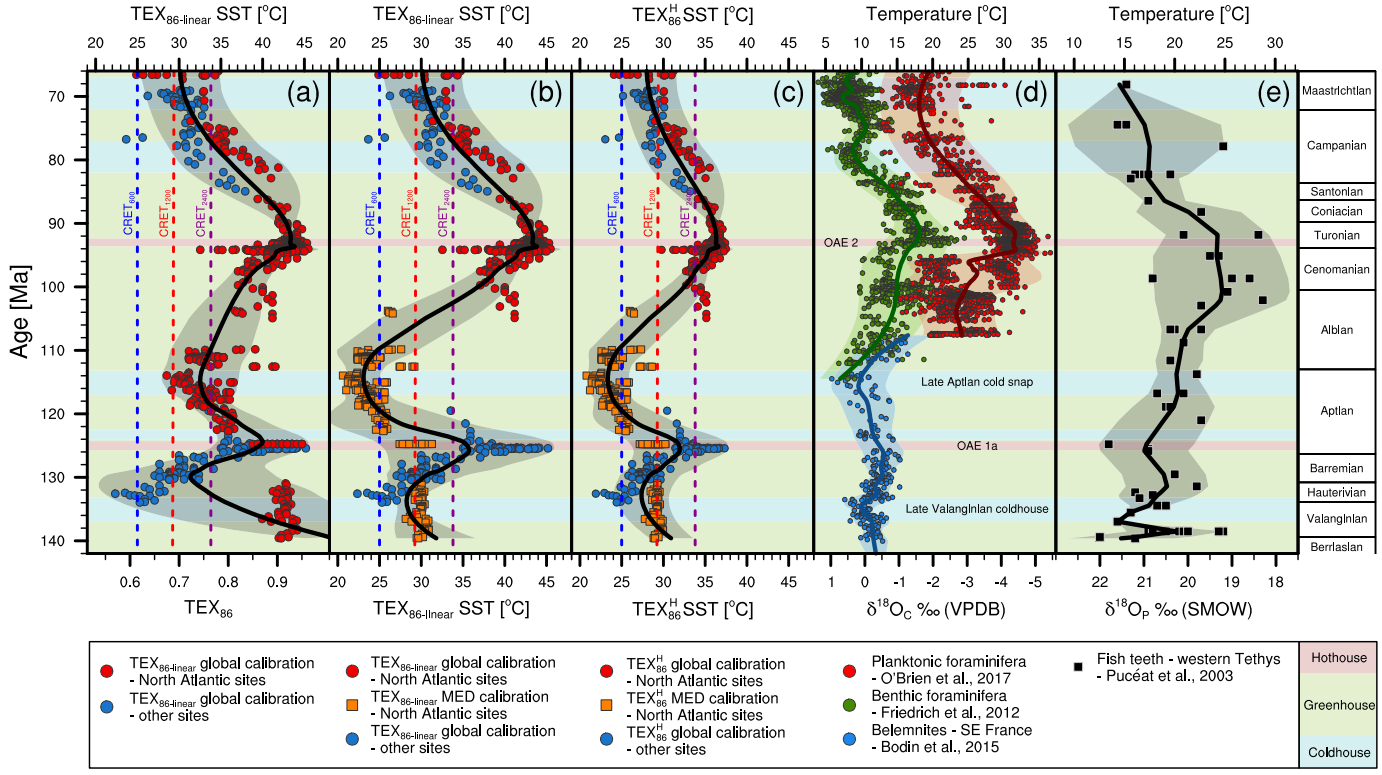

Fig. 8. Cretaceous ocean temperature evolution for different proxy archives. Panels show data for (a-c) TEX_{86} (O'Brien et al., 2017), (d) $\delta^{18}O_{carb}$ of a planktonic (O'Brien et al., 2017) and benthic compilation (Friedrich et al., 2012) as well as for belemnites from the Vocontian Basin (Bodin et al., 2015) and (e) $\delta^{18}O_{PO_4}$ of fish teeth from the western Tethyan platform (Pucéat et al., 2003). TEX_{86} and planktonic foraminiferal data are only shown for paleolatitudes between 41°S-41°N (O'Brien et al., 2017). TEX_{86} data also includes samples where no individual isoGDGT distributions were reported. An overview of all study sites is shown in Supplementary Table S1. Temperature conversion follows (a-b) the $TEX_{86-linear}$ SST calibrations based on either global or deep Mediterranean and Red Sea core-top data, i.e. Eq. (4) and Eq. (8) (see Supplementary Fig. S8), (c) as in (b) but for TEX_{86}^{H}, i.e. Eq. (2) and Eq. (7) (see Supplementary Fig. S8), and (d-e) the temperature equations (Bemis et al., 1998; Kolodny et al., 1983) with a $\delta^{18}O_{seawater}$ of -1‰ (VSMOW) for a non-glacial world. Following the previous results, the respective regional Mediterranean and Red Sea calibrations have only been applied to the Early Cretaceous North Atlantic sites (DSDP 603, DSDP 534, DSDP 398, ODP 1049 and DSDP 545). Solid lines show a LOESS fit (span = 0.25) with the 95% prediction interval indicated by the shading around it. Vertical dashed lines represent simulated early Aptian SSTs averaged between 40°S-40°N. Background shading indicates published climatic states based on compiled sedimentological, paleontological and geochemical data (Bodin et al., 2015). Ages for fish teeth data are adjusted to GTS2012 (Ogg et al., 2012).

tion in the present-day Mediterranean and Red Sea than what is reflected in the global core-top data. The following section will demonstrate the potential influence of this hypothesis on the reconstruction of local upper ocean temperatures.

Regional TEX_{86}-temperature calibrations have been developed based on deep water samples (> 1000 m) from the present-day Mediterranean and Red Sea (Kim et al., 2015). The paleowater depth estimates for the Cretaceous OAE 1a sites start at ~500 m (see Table 1). We therefore revisit the corresponding calibration data set to justify the application of these deep water calibrations to the OAE 1a data. In the modern Mediterranean and Red Sea core-top data, high correlations between TEX_{86} and both SST and 0-200 m temperatures are already observed by excluding samples from water depths < 250 m (see Supplementary Fig. S8). Shallow sediments from the upper 250 m show markedly different ring indices indicating additional non-temperature influences on the isoGDGT distribution (see Supplementary Fig. S9). Temperature calibrations omitting samples from the upper 500 m or 1000 m are very similar and significantly different to the global regressions (see Supplementary Fig. S8). For consistency to the pioneering work on the TEX_{86}-SST relation in these deep, restricted basins (Kim et al., 2015), we here apply the regional calibrations for sediments below 1000 m (Eq. (7)-(10) in Supplementary Fig. S8) but note that the results are very similar for a depth threshold of 500 m.

Application of these regional calibrations for TEX_{86}^{H} and $TEX_{86-linear}$ to DSDP sites 398 and 511 from the North and South Atlantic significantly reduces the local upper ocean temperature estimates for OAE 1a (Fig. 7). Mean SSTs are reduced by 6-8 °C for TEX_{86}^{H} and by 8-13 °C for $TEX_{86-linear}$. Absolute values of ~ 30 °C for DSDP site 398 are very similar for both calibrations because the inclusion of high TEX_{86} values from the Red Sea (up to 0.89) reduces the effect of the different extrapolation approaches visible for the global calibration. Resulting SSTs from the North Atlantic are lower than for the low-latitude Djebel Serdj location, but also in comparison to the Alstätte section located ~ 7° further to the north (see Supplementary Table S2). Respective 0-200 m integrated temperatures are lower by about 4 °C for TEX_{86}^{H} and by 6-9 °C for $TEX_{86-linear}$(Fig. 7c-d). Overall, the application of the regionally varying calibrations therefore leads to subsurface temperatures at all OAE 1a sites that are within the range between $CRET_{1200}$ and $CRET_{2400}$ for the logarithmic TEX_{86}^{H}, but closer to $CRET_{2400}$ for $TEX_{86-linear}$.

Independent validation of the proposed lower temperatures for the North and South Atlantic is challenging because of the sparse availability of additional quantitative temperature proxies. Available low- and mid-latitude TEX_{86} and oxygen isotope data uniformly show highest upper ocean temperatures around the Cenomanian-Turonian boundary and subsequent long-term cooling (Fig. 8). TEX_{86}-derived temperatures during the Cretaceous Thermal Optimum reach up to 45 °C for the linear calibration (Fig. 8a) and 37 °C for TEX_{86}^{H} (Fig. 8c), with the latter comparable to the warmest values derived from oxygen isotopes of planktonic foraminifera (Fig. 8d; O'Brien et al., 2017). High $\delta^{18}O$ values

of belemnites (Fig. 8d; Bodin et al., 2015) and fish teeth from the western Tethys (Fig. 8e; Pucéat et al., 2003) indicate overall lowest mean temperatures during the earliest Cretaceous and the Campanian-Maastrichtian interval. Similarly, TEX_{86} samples from the Boreal realm show lowest temperatures during the Early Hauterivian (TEX_{86} values around 0.6) and a gradual increase towards OAE 1a (Fig. 8a). In contrast, TEX_{86}-derived temperatures from two sites in the North Atlantic (DSDP sites 603 and 534) (Littler et al., 2011) record very warm and stable conditions over a period of about 14 million years during the Berriasian–Barremian (see Supplementary Fig. S6). $TEX_{86-linear}$ (TEX_{86}^{H}) SST estimates for these sites average at around 42 °C (36 °C) which is on par with peak OAE 1a and OAE 2 conditions and even above the extrapolated $CRET_{2400}$ temperature of 34 °C. The equivalent mean temperature change between the Valanginian minimum and OAE 2 maximum recorded in the fish teeth is significantly larger and amounts to about 10 °C, assuming no changes in the seawater fractionation. A similar decrease in $\delta^{18}O$ of 2-3‰ is also visible between Albian and Turonian values in a compilation of benthic foraminifera (Fig. 8d; Friedrich et al., 2012). Applying the Mediterranean and Red Sea calibrations to Early Cretaceous TEX_{86} samples from the North Atlantic (Fig. 8b-c) reduces the observed spread during the earliest Cretaceous significantly and increases the amplitude of the Late Aptian cold snap. In agreement to the belemnite record, resulting minimum values for the Late Aptian cold snap and Late Valanginian coldhouse are similar and around low- to mid-latitude $CRET_{600}$ temperatures (40°S-40°N). With the exception of the OAE 1a interval, TEX_{86}-derived temperatures are within the range of model simulations forced with 600 and 1200 ppmv atmospheric CO_2 throughout the Early Cretaceous, which is consistent with low-resolution background CO_2 estimates (Foster et al., 2017; Jing and Bainian, 2018) and high-resolution OAE 1a reconstructions (Naafs et al., 2016).

4. Discussion

4.1. Consistency of the OAE 1a TEX_{86} record

Our simulations reveal an improved model-data fit for the early Aptian OAE 1a temperatures by applying the 0-200 m depth-integrated calibrations, compared to the sea surface calibrations. The reconstructed temperatures based on the deep subsurface calibration are overall closest to $CRET_{1200}$. This enhanced model-proxy congruence has also been shown for the early Eocene (Ho and Laepple, 2016) but the ecological justification of this statistical approach remains under debate (Tierney et al., 2017; Ho and Laepple, 2017). Based on modern core-top data, a recent study concluded that the TEX_{86} signal is generated within the upper 200 m (Zhang and Liu, 2018). We show that our model results for this depth range are only consistent with the OAE 1a TEX_{86} record when we apply regionally varying temperature calibrations that reduce the absolute temperatures in the Early Cretaceous North and South Atlantic. Under this hypothesis, reconstructed OAE 1a surface temperatures are broadly consistent with the model results for the reconstructed CO_2 range between 1200 and 2400 ppmv. An exception to this are the SSTs derived from the $TEX_{86-linear}$ calibration. The global calibration yields temperature estimates uniformly above simulated peak OAE 1a temperatures, even in the West Pacific Warm Pool. This might indicate an overestimation of the extrapolated temperatures for TEX_{86} values outside of the modern calibration range or an underestimation of the climate sensitivity in our model. We note that the model-data congruence is improved for the application of the logarithmic TEX_{86}^{H}, even though there is no ecological reasoning for the reduced TEX_{86}-SST sensitivity at the high end of the calibration (Wuchter et al., 2004; Schouten et al., 2007; Kim et al., 2010).

The inter-site comparison of available proxy data with regard to results from the physical ocean model allows an approach to test the TEX_{86} records irrespective of a temperature calibration. During the Early Cretaceous, paleogeographic reconstructions place ODP site 1207 and DSDP site 463 into the equatorial central to western Pacific (Schouten et al., 2003; Dumitrescu et al., 2006; O'Brien et al., 2017), a region that forms the Western Pacific Warm Pool both in modern observations and our Cretaceous simulations. The Warm Pool is mainly caused by the westward blowing trade winds piling up the warm surface waters in the central and western part of the basin. The resulting shoaling of the thermocline in the east leads to upwelling of cooler waters off the coast of South America and produces a strong zonal gradient of upper ocean temperatures along the equator (Clement et al., 2005). Based on this reasoning, TEX_{86} values from the Warm Pool region should also be the highest globally for OAE 1a. It is therefore surprising that TEX_{86} values at DSPS site 398 in the North Atlantic are on average even slightly higher than those in the Pacific Warm Pool. Our proposed different TEX_{86}-SST relation for the young North Atlantic would be a possible explanation for this observation. On the other hand, resulting absolute temperatures for DSDP site 398 are even lower than reconstructions for the more northern Alstätte section from the Lower Saxony Basin. We can exclude that this record was influenced by a similar contribution of deeper living Thaumarchaeota communities due to the estimated shallow paleowater depth of below 200 m (Bottini and Mutterlose, 2012). This might indicate that the magnitude of the proposed warm bias at DSDP site 398 is overestimated in our analysis, especially for $TEX_{86-linear}$. Another possibility might be that the 4 included TEX_{86} samples from Alstätte represent the peak warming phase of OAE 1a rather than the mean conditions.

4.2. Reasons for the systematic isoGDGT differences

The comparison of the isoGDGT distributions reveals a general increase in the relative proportions of [Cren'] and [GDGT-2] in samples from the Early Cretaceous North and South Atlantic compared to other Cretaceous data, even after applying a strict GDGT screening for potential secondary influences (see Section 2.4). Resulting $f_{(Cren'+GDGT-2)/Cren}$ ratios for the Early Cretaceous Atlantic Ocean are characterised by a stronger increase with TEX_{86} than for the Late Cretaceous group. The $f_{(Cren'+GDGT-2)/Cren}$-TEX_{86} relation is also different from that found in the extrapolated global core-top data and rather shows similarities to sediments from the deep Mediterranean and Red Sea, where the sedimentary isoGDGT signal is influenced by an enhanced contribution of a deep-water Thaumarchaeota community (Kim et al., 2015, 2016). We therefore argue that a similar water-depth influence might explain parts of the systematic isoGDGT differences in the Cretaceous Atlantic Ocean data. The exact reasons for this water-depth control on the TEX_{86} signal in these marine settings are still not clear (Villanueva et al., 2015; Kim et al., 2015, 2016). One hypothesis put forward (Kim et al., 2015) is that the warm intermediate and bottom water temperatures in these restricted basins lead to higher ammonium generation rates due to increased organic matter mineralisation. This might increase the abundance of the nitrifying Thaumarchaeota in deeper waters and therefore enhance their contribution to the sedimentary TEX_{86} signal. It is also possible that the warm and saline waters promote the preservation and export of membrane lipids of the deep-water Thaumarchaeota (Kim et al., 2016) or lead to the presence of endemic populations in these restricted environments (Trommer et al., 2009). Besseling et al. (2019) found unusually high subsurface abundances of Thaumarchaeota in the upper 500 m of the Mediterranean Sea compared to the North Atlantic. Gene sequencing indicates a potential adaptation of these deeper Thaumarchaeota communities to the presence of particularly warm

and saline intermediate waters (Besseling et al., 2019). In accordance, our simulations reveal that the oceanographic setting of the Early Cretaceous North and South Atlantic was more similar to the modern Mediterranean Sea than to open-ocean conditions. Mean evaporation exceeded precipitation and formed warm and saline intermediate and bottom waters that filled the silled basins.

Physiological controls on TEX_{86} have been demonstrated in culture studies (Elling et al., 2014; Qin et al., 2015; Hurley et al., 2016) that show an inverse relation between ammonia oxidation rates and TEX_{86} (Hurley et al., 2016). Consequently, regional differences in the organic matter export and remineralisation significantly change the vertical structure of the water column TEX_{86} temperatures for the present day (Hurley et al., 2018). On longer time scales, earth system modelling indicates the potential for severe changes in the marine nitrogen cycle in deoxygenated ocean basins (Naafs et al., 2019). The proposed transition from a nitrate-dominated to an ammonium-dominated fixed nitrogen inventory during OAE 2 has the potential to influence the depth habitat of nitrifying Thaumarchaeota (Naafs et al., 2019). Changes in global nutrient cycles and budgets therefore need to be considered to assess potentially variable ecological influences on the TEX_{86}-temperature relation in the geologic record (Hurley et al., 2016, 2018), especially in the restricted and deoxygenated basins of the Cretaceous.

4.3. Ocean circulation in the Early Cretaceous North and South Atlantic

Water mass exchange in the opening South Atlantic was severely restricted by the Falkland Plateau (Pérez-Díaz and Eagles, 2017; Dummann et al., 2020) and the shallow depth of the proto-Drake Passage (Donnadieu et al., 2016). Simulated water masses at DSDP site 511 were dominated by surface inflow of cool and fresh Southern Ocean waters and a southward subsurface return flow of warm and saline South Atlantic Intermediate Water. This anti-estuarine circulation bears a resemblance to the modern Strait of Gibraltar and the Portuguese continental margin where a strong warm bias in TEX_{86}^{H}-derived temperatures has been attributed to the presence of the warm and saline Mediterranean Outflow Water (Kim et al., 2016).

In contrast, the North Atlantic was characterised by an estuarine circulation with a wind-driven zonal surface water export to the Pacific Ocean and intermediate water inflow via the Central American Seaway (Trabucho-Alexandre et al., 2012). The narrow proto-Caribbean ocean, small island arcs between North and South America (Ross and Scotese 1988) and the still closed equatorial Atlantic passage (Sewall et al., 2007) severely limited intermediate water exchange with the Pacific during the Early Cretaceous. In our simulations and in accordance with other available reconstructions for the early Aptian (Sewall et al., 2007), the North Atlantic was effectively isolated from the global deep-water circulation below 1200 m. This geographical restriction favoured the local formation of warm and saline deep waters.

While quantitative reconstructions of the circulation in the young Atlantic Ocean are complicated by the still limited knowledge about paleogeographic boundary conditions, previous studies support the idea of limited connectivity to surrounding basins. Conspicuously cool Aptian-Albian surface temperatures derived from oxygen isotopes of planktonic foraminifera from the subtropical North Atlantic have been interpreted to reflect a high-evaporative fractionation factor influencing local seawater composition (Huber et al., 2011). Absolute water mass exchange of the North Atlantic with adjacent basins, diagnosed from corresponding anomalous strontium isotopic values, might have been even lower than the modern day transport between the Mediterranean Sea and the Atlantic Ocean (Huber et al., 2011). While this might be a rather extreme estimate, other climate model simulations also show locally formed warm and saline intermediate and deep waters (Barron and Peterson, 1990), primarily driven by the local geographic confinement (Poulsen et al., 2001). The resulting low vertical temperature gradient is also evident in the South Atlantic in the form of virtually identical oxygen isotope values for planktonic and benthic foraminifera at the Falkland Plateau during the Aptian/Albian boundary interval (Huber et al., 2018). $\delta^{18}O$-derived benthic temperatures for the Albian range between 8-12 °C (Huber et al., 2018) and therefore lie between $CRET_{600}$ and $CRET_{1200}$ bottom water temperatures. In addition, sub-thermocline Barremian-Aptian temperatures of 10-16 °C, based on oxygen-isotope ratios of belemnites from the Falkland Plateau (Price and Gröcke, 2002) are also very similar to deep-water temperatures in $CRET_{1200}$ and the modern Mediterranean Sea (Locarnini et al., 2013).

4.4. Differences between Early and Late Cretaceous isoGDGTs

The reduced fractional abundances of [Cren'] and [GDGT-2] and increases in [Cren] in Late Cretaceous samples from the North Atlantic allow for two possible explanations. First, temporal changes might simply arise by chance due to different sampling locations. This would imply that the processes leading to the enhanced subsurface influence are limited only to certain regions of the North Atlantic or Late Cretaceous sites are situated at too shallow water depths to record any contribution of deep-dwelling Thaumarchaeota. Indeed, we note that the Early Cretaceous sites are rather clustered towards the probably more restricted (Arthur and Natland, 1979) northern and eastern parts of the North Atlantic, while most younger records are situated closer to the equator or western part of the basin (O'Brien et al., 2017). The overall reduced [GDGT-2]/[GDGT-3] ratios of the Late Cretaceous samples could also indicate shallower paleowater depths (Taylor et al., 2013). While Late Cretaceous sites with very shallow water depths (e.g. Bass River, Meirs Farm or Brazos River; see Supplementary Table S1) exclude per se any influence of deeper living archaeal communities, we also find no suspicious isoGDGT distributions at site DSDP 367 (Schouten et al., 2003; Forster et al., 2007) with a paleowater depth below 3000 m (Lancelot et al., 1978). The relative large number and random selection of the locations forming the Early and Late Cretaceous groups in this analysis could also indicate a common underlying mechanism that led to a temporal change of the large-scale oceanographic setting. We hypothesise that enhanced intermediate and deep-water exchange with adjacent basins and the gradual shift from a highly restricted to a more ventilated Atlantic Ocean led to a progressive decline of the subsurface influence (up to 1000 m in the modern Mediterranean Sea (Kim et al., 2015)) on the sedimentary TEX_{86} signal. The opening of the equatorial Atlantic gateway during the mid-Cretaceous (Pérez-Díaz and Eagles, 2017) allowed for enhanced water mass flow between the North and South Atlantic and might explain the observed transient changes in isoGDGT distributions. While a full deep water passage was probably not established before the Campanian (Friedrich and Erbacher, 2006), a shallow and maybe even intermediate water connection might have been present since 100 Ma (Pérez-Díaz and Eagles, 2017). Model simulations show a drop of the North Atlantic intermediate water temperature (salinity) at 1500 m depth of about 7 °C (0.5) between the Albian and Turonian times solely because of changes in the paleogeography (Poulsen et al., 2001) and enhanced inflow of Southern Ocean sourced waters (Donnadieu et al., 2016). The gradual widening of the proto-Caribbean ocean throughout the Early Cretaceous (Ross and Scotese, 1988) might have additionally increased the advection of cooler Pacific intermediate water into the North Atlantic (Topper et al., 2011). The resulting decrease in intermediate water temperatures and salinities potentially reduced the unusually high influence of the deep-dwelling Thaumarchaeota observed during the Early Cretaceous.

A potential enhanced influence of deep-water Thaumarchaeota communities on the sedimentary TEX_{signal} would also mean that the warm bias for the Early Cretaceous varies with the respective paleowater depth at each site. Given the large uncertainty in these estimates for deep-time periods (Table 1), this further complicates the reconstruction of absolute temperatures. Areas outside of the restricted North and South Atlantic are therefore probably more suitable for assessing the mean ocean temperature evolution and could reveal valuable information about the strength and transient nature of any regional TEX_{86} warm bias. This becomes even more important as the vast majority of available Cretaceous TEX_{86} data are derived from the North Atlantic (O'Brien et al., 2017) due to the subduction-related loss of sediments from other ocean basins.

5. Conclusions

Based on two independent lines of evidence resulting from physical circulation modelling and the systematic comparison of Cretaceous and modern isoGDGT distributions we conclude that:

- Early Cretaceous North and South Atlantic isoGDGT samples show a systematic increase in the relative abundance of [Cren'] and [GDGT-2] with a simultaneous decrease in [Cren] compared to other Cretaceous data. As the derived TEX_{86} ratio does not include [Cren], this potentially influences resulting Early Cretaceous TEX_{86} values and the regional TEX_{86}-temperature relation.
- We expect that this offset is caused by an enhanced contribution of deep-water archaeal communities with a different isoGDGT distribution influencing the sedimentary TEX_{86} signal that is similar to observations from the modern Mediterranean and Red Sea.
- General circulation modelling shows the local formation of warm and saline intermediate and deep waters in the restricted North and South Atlantic Ocean that may have provided ideal environmental conditions for deep-water dwelling Thaumarchaeota.
- Applying a regional temperature calibration from the modern Mediterranean and Red Sea to the respective Cretaceous data reduces reconstructed upper ocean temperatures by 4-13 °C.
- Resulting OAE 1a subsurface (0-200 m) temperatures are broadly consistent with model results at the reconstructed CO_2 range of 1200 to 2400 ppmv.
- Potential regional and temporal changes of the TEX_{86}-temperature relation should be considered when interpreting the TEX_{86} paleorecord of restricted basins

Clearly, our approach of applying the modern Mediterranean and Red Sea calibration to parts of the Cretaceous data can only be considered a rather rough first approximation under the assumption that TEX_{86} export dynamics were comparable. Independent evidence from other proxies will be essential to confirm and also constrain any regional or temporal deviations of the TEX_{86}-temperature relation from current global core-top calibrations. Furthermore, it will be necessary to better understand the spatial differences in present-day TEX_{86} export dynamics and what secondary processes besides temperature influence the isoGDGT distributions in the modern core-top data, especially in deep restricted basins. But whatever the exact reasons for the observed differences in the isoGDGT patterns might be, our results demonstrate the need to apply regionally varying temperature calibrations that reflect the differences in the sedimentary TEX_{86} signal also for deep-time periods like the Cretaceous. Approaches that specifically incorporate the spatial structure of the present-day regression parameters have been proposed (Tierney and Tingley, 2014, 2015), but are not directly transferable to time periods like the Cretaceous due to the vastly different land-sea configuration and environmental conditions. Instead, analogue predictions have been developed (Tierney and Tingley, 2014) and estimate deep-time temperatures based on similarities of TEX_{86} values alone. Our study suggests that a pattern analysis of the whole isoGDGT space might reveal even more information about the local export dynamics than what is encoded in the derived TEX_{86} ratio. The "manual" approach in this study and new "automated" machine-learning techniques (Eley et al., 2019) to compare modern and past isoGDGT distributions are a potential way forward to address the question whether present-day analogue environments for isoGDGT assemblages of past greenhouse periods exist, and if so, where we can find them.

Acknowledgements

This research used samples provided by the Deep Sea Drilling Project (DSDP). We further thank the German Research Foundation (DFG) for funding this research within the project "Evolving carbon sinks in the young South Atlantic: Drivers of global climate in the early Cretaceous greenhouse?" (grant numbers FL378/1-1, FL378/1-2 and HO2188/9). S.F. has been additionally supported by the German Research Foundation through the collaborative research project SFB 754 (sub-project A7). This is a contribution to PalMod. Model integrations were conducted at the Computing Center of Kiel University. We thank Janine Blöhdorn for generating most of the Cretaceous boundary conditions for the model and Stefan Hagemann for constructing the parameters for the hydrological discharge model. We are also grateful to Oliver Friedrich for providing the compilation of benthic foraminifera oxygen isotopic data and thank David Naafs for sharing the GDGT data from Djebel Serdj.

Appendix A. Supplementary material

Supplementary material related to this article can be found online at https://doi.org/10.1016/j.epsl.2020.116184.

References

Arthur, M.A., Natland, J.H., 1979. Carbonaceous sediments in the North and South Atlantic: the role of salinity in stable stratification of early Cretaceous basins. In: Deep Drilling Results in the Atlantic Ocean: Continental Margins and Paleoenvironment, vol. 3, pp. 375–401.

Barron, E.J., 1983. A warm, equable Cretaceous: the nature of the problem. Earth-Sci. Rev. 19, 305–338. https://doi.org/10.1016/0012-8252(83)90001-6.

Barron, E.J., Peterson, W.H., 1990. Mid-Cretaceous ocean circulation: results from model sensitivity studies. Paleoceanography 5, 319–337. https://doi.org/10.1029/PA005i003p00319.

Bemis, B.E., Spero, H.J., Bijma, J., Lea, D.W., 1998. Reevaluation of the oxygen isotopic composition of planktonic foraminifera: experimental results and revised paleotemperature equations. Paleoceanography 13, 150–160. https://doi.org/10.1029/98PA00070.

Besseling, M.A., Hopmans, E.C., Koenen, M., van der Meer, M.T., Vreugdenhil, S., Schouten, S., Sinninghe Damsté, J.S., Villanueva, L., 2019. Depth-related differences in archaeal populations impact the isoprenoid tetraether lipid composition of the Mediterranean Sea water column. Org. Geochem. 135, 16–31. https://doi.org/10.1016/j.orggeochem.2019.06.008.

Blakey, R.C., 2008. Gondwana paleogeography from assembly to breakup—a 500 m.y. odyssey. In: Special Paper 441: Resolving the Late Paleozoic Ice Age in Time and Space, vol. 441. Geological Society of America, pp. 1–28.

Blöhdorn, J., 2013. Klima und Ozeanzirkulation der Frühen Kreide im Kiel Climate Model. PhD thesis. Christian-Albrechts-Universität Kiel.

Bodin, S., Meissner, P., Janssen, N.M., Steuber, T., Mutterlose, J., 2015. Large igneous provinces and organic carbon burial: controls on global temperature and continental weathering during the Early Cretaceous. Glob. Planet. Change 133, 238–253. https://doi.org/10.1016/j.gloplacha.2015.09.001.

Bottini, C., Erba, E., Tiraboschi, D., Jenkyns, H.C., Schouten, S., Sinninghe Damsté, J.S., 2015. Climate variability and ocean fertility during the Aptian Stage. Clim. Past 11, 383–402. https://doi.org/10.5194/cp-11-383-2015.

Bottini, C., Mutterlose, J., 2012. Integrated stratigraphy of early aptian black shales in the boreal realm: calcareous nannofossil and stable isotope evidence for global and regional processes. Newsl. Stratigr. 45, 115–137. https://doi.org/10.1127/0078-0421/2012/0017.

Bralower, T.J., Silva, I.P., Malone, M.J., 2002. New evidence for abrupt climate change in the Cretaceous and Paleogene: an ocean drilling program expedition to Shatsky Rise, northwest Pacific. GSA Today 12, 4–10. https://doi.org/10.1130/1052-5173(2002)012<0004:NEFACC>2.0.CO;2.

Castañeda, I.S., Schefuß, E., Pätzold, J., Sinninghe Damsté, J.S., Weldeab, S., Schouten, S., 2010. Millennial-scale sea surface temperature changes in the eastern Mediterranean (Nile River Delta region) over the last 27,000 years. Paleoceanography 25, 1–13. https://doi.org/10.1029/2009PA001740.

Clement, A.C., Seager, R., Murtugudde, R., 2005. Why are there tropical warm pools? J. Climate 18, 5294–5311. https://doi.org/10.1175/JCLI3582.1.

Donnadieu, Y., Pucéat, E., Moiroud, M., Guillocheau, F., Deconinck, J.F., 2016. A better-ventilated ocean triggered by Late Cretaceous changes in continental configuration. Nat. Commun. 7. https://doi.org/10.1038/ncomms10316.

Dumitrescu, M., Brassell, S.C., Schouten, S., Hopmans, E.C., Sinninghe Damsté, J.S., 2006. Instability in tropical Pacific sea-surface temperatures during the early Aptian. Geology 34, 833–836. https://doi.org/10.1130/G22882.1.

Dummann, W., Steinig, S., Hofmann, P., Flögel, S., Osborne, A., Frank, M., Herrle, J., Bretschneider, L., Sheward, R., Wagner, T., 2020. The impact of Early Cretaceous gateway evolution on ocean circulation and organic carbon burial in the emerging South Atlantic and Southern Ocean basins. Earth Planet. Sci. Lett. 530, 115890. https://doi.org/10.1016/j.epsl.2019.115890.

Eley, Y.L., Thompson, W., Greene, S.E., Mandel, I., Edgar, K., Bendle, J.A., Dunkley Jones, T., 2019. OPTiMAL: a new machine learning approach for GDGT-based palaeothermometry. Clim. Past Discuss., 1–39. https://doi.org/10.5194/cp-2019-60.

Elling, F.J., Könneke, M., Lipp, J.S., Becker, K.W., Gagen, E.J., Hinrichs, K.U., 2014. Effects of growth phase on the membrane lipid composition of the thaumarchaeon Nitrosopumilus maritimus and their implications for archaeal lipid distributions in the marine environment. Geochim. Cosmochim. Acta 141, 579–597. https://doi.org/10.1016/j.gca.2014.07.005.

Forster, A., Schouten, S., Moriya, K., Wilson, P.A., Sinninghe Damsté, J.S., 2007. Tropical warming and intermittent cooling during the Cenomanian/Turonian oceanic anoxic event 2: Sea surface temperature records from the equatorial Atlantic. Paleoceanography 22 (1). https://doi.org/10.1029/2006PA001349.

Foster, G.L., Royer, D.L., Lunt, D.J., 2017. Future climate forcing potentially without precedent in the last 420 million years. Nat. Commun. 8, 14845. https://doi.org/10.1038/ncomms14845.

Friedrich, O., Erbacher, J., 2006. Benthic foraminiferal assemblages from Demerara Rise (ODP Leg 207, western tropical Atlantic): possible evidence for a progressive opening of the Equatorial Atlantic Gateway. Cretac. Res. 27, 377–397. https://doi.org/10.1016/j.cretres.2005.07.006.

Friedrich, O., Norris, R.D., Erbacher, J., 2012. Evolution of middle to late Cretaceous oceans-a 55 m.y. record of Earth's temperature and carbon cycle. Geology 40, 107–110. https://doi.org/10.1130/G32701.1.

Hagemann, S., Dümenil, L., 1998. A parametrization of the lateral waterflow for the global scale. Clim. Dyn. 14, 17–31. https://doi.org/10.1007/s003820050205.

Heldt, M., Bachmann, M., Lehmann, J., 2008. Microfacies, biostratigraphy, and geochemistry of the hemipelagic Barremian-Aptian in north-central Tunisia: influence of the OAE 1a on the southern Tethys margin. Palaeogeogr. Palaeoclimatol. Palaeoecol. 261, 246–260. https://doi.org/10.1016/j.palaeo.2008.01.013.

Ho, S.L., Laepple, T., 2016. Flat meridional temperature gradient in the early Eocene in the subsurface rather than surface ocean. Nat. Geosci. 9, 606–610. https://doi.org/10.1038/ngeo2763.

Ho, S.L., Laepple, T., 2017. Reply to 'Eocene temperature gradients'. Nat. Geosci. 10, 539–540. https://doi.org/10.1038/ngeo2998.

Holbourn, A., Kuhnt, W., Soeding, E., 2001. Atlantic paleobathymetry, paleoproductivity and paleocirculation in the late Albian: the benthic foraminiferal record. Palaeogeogr. Palaeoclimatol. Palaeoecol. 170, 171–196. https://doi.org/10.1016/S0031-0182(01)00223-1.

Hollis, C.J., Dunkley Jones, T., Anagnostou, E., Bijl, P.K., Cramwinckel, M.J., Cui, Y., Dickens, G.R., Edgar, K.M., Eley, Y., Evans, D., Foster, G.L., Frieling, J., Inglis, G.N., Kennedy, E.M., Kozdon, R., Lauretano, V., Lear, C.H., Littler, K., Lourens, L., Meckler, A.N., Naafs, B.D.A., Pälike, H., Pancost, R.D., Pearson, P.N., Röhl, U., Royer, D.L., Salzmann, U., Schubert, B.A., Seebeck, H., Sluijs, A., Speijer, R.P., Stassen, P., Tierney, J., Tripati, A., Wade, B., Westerhold, T., Witkowski, C., Zachos, J.C., Zhang, Y.G., Huber, M., Lunt, D.J., 2019. The DeepMIP contribution to PMIP4: methodologies for selection, compilation and analysis of latest Paleocene and early Eocene climate proxy data, incorporating version 0.1 of the DeepMIP database. Geosci. Model Dev. 12, 3149–3206. https://doi.org/10.5194/gmd-12-3149-2019.

Hollis, C.J., Taylor, K.W., Handley, L., Pancost, R.D., Huber, M., Creech, J.B., Hines, B.R., Crouch, E.M., Morgans, H.E., Crampton, J.S., Gibbs, S., Pearson, P.N., Zachos, J.C., 2012. Early Paleogene temperature history of the Southwest Pacific Ocean: reconciling proxies and models. Earth Planet. Sci. Lett. 349–350, 53–66. https://doi.org/10.1016/j.epsl.2012.06.024.

Hopmans, E.C., Schouten, S., Sinninghe Damsté, J.S., 2016. The effect of improved chromatography on GDGT-based palaeoproxies. Org. Geochem. 93, 1–6. https://doi.org/10.1016/j.orggeochem.2015.12.006.

Hopmans, E.C., Weijers, J.W., Schefuß, E., Herfort, L., Sinninghe Damsté, J.S., Schouten, S., 2004. A novel proxy for terrestrial organic matter in sediments based on branched and isoprenoid tetraether lipids. Earth Planet. Sci. Lett. 224, 107–116. https://doi.org/10.1016/j.epsl.2004.05.012.

Huber, B.T., MacLeod, K.G., Gröcke, D.R., Kucera, M., 2011. Paleotemperature and paleosalinity inferences and chemostratigraphy across the Aptian/Albian boundary in the subtropical North Atlantic. Paleoceanography 26. https://doi.org/10.1029/2011PA002178.

Huber, B.T., MacLeod, K.G., Watkins, D.K., Coffin, M.F., 2018. The rise and fall of the Cretaceous Hot Greenhouse climate. Glob. Planet. Change 167, 1–23. https://doi.org/10.1016/j.gloplacha.2018.04.004.

Hurley, S.J., Elling, F.J., Könneke, M., Buchwald, C., Wankel, S.D., Santoro, A.E., Lipp, J.S., Hinrichs, K.U., Pearson, A., 2016. Influence of ammonia oxidation rate on thaumarchaeal lipid composition and the TEX 86 temperature proxy. Proc. Natl. Acad. Sci. 113, 7762–7767. https://doi.org/10.1073/pnas.1518534113.

Hurley, S.J., Lipp, J.S., Close, H.G., Hinrichs, K.U., Pearson, A., 2018. Distribution and export of isoprenoid tetraether lipids in suspended particulate matter from the water column of the Western Atlantic Ocean. Org. Geochem. 116, 90–102. https://doi.org/10.1016/j.orggeochem.2017.11.010.

Jenkyns, H.C., 2010. Geochemistry of oceanic anoxic events. Geochem. Geophys. Geosyst. 11, 1–30. https://doi.org/10.1029/2009GC002788.

Jenkyns, H.C., Schouten-Huibers, L., Schouten, S., Sinninghe Damsté, J.S., 2012. Warm Middle Jurassic-Early Cretaceous high-latitude sea-surface temperatures from the Southern Ocean. Clim. Past 8, 215–225. https://doi.org/10.5194/cp-8-215-2012.

Jing, D., Bainian, S., 2018. Early Cretaceous atmospheric CO2 estimates based on stomatal index of Pseudofrenelopsis papillosa (Cheirolepidiaceae) from southeast China. Cretac. Res. 85, 232–242. https://doi.org/10.1016/j.cretres.2017.08.011.

Kim, J.H., van der Meer, J., Schouten, S., Helmke, P., Willmott, V., Sangiorgi, F., Koç, N., Hopmans, E.C., Damsté, J.S.S., 2010. New indices and calibrations derived from the distribution of crenarchaeal isoprenoid tetraether lipids: implications for past sea surface temperature reconstructions. Geochim. Cosmochim. Acta 74, 4639–4654. https://doi.org/10.1016/j.gca.2010.05.027.

Kim, J.H., Romero, O.E., Lohmann, G., Donner, B., Laepple, T., Haam, E., Sinninghe Damsté, J.S., 2012. Pronounced subsurface cooling of North Atlantic waters off Northwest Africa during Dansgaard-Oeschger interstadials. Earth Planet. Sci. Lett. 339–340, 95–102. https://doi.org/10.1016/j.epsl.2012.05.018.

Kim, J.H., Schouten, S., Hopmans, E.C., Donner, B., Sinninghe Damsté, J.S., 2008. Global sediment core-top calibration of the TEX86 paleothermometer in the ocean. Geochim. Cosmochim. Acta 72, 1154–1173. https://doi.org/10.1016/j.gca.2007.12.010.

Kim, J.H., Schouten, S., Rodrigo-Gámiz, M., Rampen, S., Marino, G., Huguet, C., Helmke, P., Buscail, R., Hopmans, E.C., Pross, J., Sangiorgi, F., Middelburg, J.B.M., Sinninghe Damsté, J.S., 2015. Influence of deep-water derived isoprenoid tetraether lipids on the TEX86H paleothermometer in the Mediterranean Sea. Geochim. Cosmochim. Acta 150, 125–141. https://doi.org/10.1016/j.gca.2014.11.017.

Kim, J.H., Villanueva, L., Zell, C., Sinninghe Damsté, J.S., 2016. Biological source and provenance of deep-water derived isoprenoid tetraether lipids along the Portuguese continental margin. Geochim. Cosmochim. Acta 172, 177–204. https://doi.org/10.1016/j.gca.2015.09.010.

Kolodny, Y., Luz, B., Navon, O., 1983. Oxygen isotope variations in phosphate of biogenic apatites, I. Fish bone apatite-rechecking the rules of the game. Earth Planet. Sci. Lett. 64, 398–404. https://doi.org/10.1016/0012-821X(83)90100-0.

Lancelot, Y., Seibold, E., Lancelot, Y., 1978. The Evolution of the Central Northeastern Atlantic - Summary of Results of DSDP Leg 41. Initial Reports of the Deep Sea Drilling Project, 41.

Littler, K., Robinson, S.A., Bown, P.R., Nederbragt, A.J., Pancost, R.D., 2011. High sea-surface temperatures during the Early Cretaceous Epoch. Nat. Geosci. 4, 169–172. https://doi.org/10.1038/ngeo1081.

Locarnini, R.A., Mishonov, A.V., Antonov, J.I., Boyer, T.P., Garcia, H.E., Baranova, O.K., Zweng, M.M., Paver, C.R., Reagan, J.R., Johnson, D.R., Hamilton, M., Seidov, D., 2013. World ocean atlas 2013, vol. 1: temperature. In: NOAA Atlas NESDIS 73. 40 pp.

Madec, G., 2008. NEMO ocean engine. In: Note du Pôle de modélisation 27. Institut Pierre-Simon Laplace (IPSL), France.

Müller, R.D., Sdrolias, M., Gaina, C., Steinberger, B., Heine, C., 2008. Long-term sea-level fluctuations driven by ocean basin dynamics. Science 319, 1357–1362. https://doi.org/10.1126/science.1151540.

Mutterlose, J., Bottini, C., Schouten, S., Sinninghe Damsté, J.S., 2014. High sea-surface temperatures during the early Aptian Oceanic Anoxic Event 1a in the Boreal Realm. Geology 42, 439–442. https://doi.org/10.1130/G35394.1.

Naafs, B.D.A., Pancost, R.D., 2016. Sea-surface temperature evolution across Aptian Oceanic Anoxic Event 1a. Geology 44, 959–962. https://doi.org/10.1130/G38575.1.

Naafs, B.D.A., Castro, J.M., De Gea, G.A., Quijano, M.L., Schmidt, D.N., Pancost, R.D., 2016. Gradual and sustained carbon dioxide release during Aptian Oceanic Anoxic Event 1a. Nat. Geosci. 9, 135–139. https://doi.org/10.1038/ngeo2627.

Naafs, B.D.A., Monteiro, F.M., Pearson, A., Higgins, M.B., Pancost, R.D., Ridgwell, A., 2019. Fundamentally different global marine nitrogen cycling in response to

severe ocean deoxygenation. Proc. Natl. Acad. Sci. 116, 24979–24984. https://doi.org/10.1073/pnas.1905553116.

O'Brien, C.L., Robinson, S.A., Pancost, R.D., Sinninghe Damsté, J.S., Schouten, S., Lunt, D.J., Alsenz, H., Bornemann, A., Bottini, C., Brassell, S.C., Farnsworth, A., Forster, A., Huber, B.T., Inglis, G.N., Jenkyns, H.C., Linnert, C., Littler, K., Markwick, P., McAnena, A., Mutterlose, J., Naafs, B.D.A., Püttmann, W., Sluijs, A., van Helmond, N.A., Vellekoop, J., Wagner, T., Wrobel, N.E., 2017. Cretaceous sea-surface temperature evolution: constraints from TEX86 and planktonic foraminiferal oxygen isotopes. Earth-Sci. Rev. 172, 224–247. https://doi.org/10.1016/j.earscirev.2017.07.012.

Ogg, J., Hinnov, L., Huang, C., 2012. Cretaceous. In: The Geologic Time Scale, vol. 1–2, pp. 793–853.

Park, W., Keenlyside, N., Latif, M., Ströh, A., Redler, R., Roeckner, E., Madec, G., 2009. Tropical Pacific climate and its response to global warming in the Kiel Climate Model. J. Climate 22, 71–92. https://doi.org/10.1175/2008JCLI2261.1.

Pérez-Díaz, L., Eagles, G., 2017. South Atlantic paleobathymetry since early Cretaceous. Sci. Rep. 7. https://doi.org/10.1038/s41598-017-11959-7.

Polik, C.A., Elling, F.J., Pearson, A., 2018. Impacts of Paleoecology on the TEX86 sea surface temperature proxy in the Pliocene-Pleistocene Mediterranean Sea. Paleoceanogr. Paleoclimatol. 33, 1472–1489. https://doi.org/10.1029/2018PA003494.

Poulsen, C.J., Barron, E.J., Arthur, M.A., Peterson, W.H., 2001. Response of the Mid-Cretaceous global oceanic circulation to tectonic and CO2 forcings. Paleoceanography 16, 576–592. https://doi.org/10.1029/2000PA000579.

Price, G.D., Gröcke, D.R., 2002. Strontium-isotope stratigraphy and oxygen- and carbon-isotope variation during the Middle Jurassic-Early Cretaceous of the Falkland Plateau, South Atlantic. Palaeogeogr. Palaeoclimatol. Palaeoecol. 183, 209–222. https://doi.org/10.1016/S0031-0182(01)00486-2.

Pucéat, E., Lécuyer, C., Sheppard, S.M.F., Dromart, G., Reboulet, S., Grandjean, P., 2003. Thermal evolution of Cretaceous Tethyan marine waters inferred from oxygen isotope composition of fish tooth enamels. Paleoceanography 18. https://doi.org/10.1029/2002PA000823.

Qin, W., Carlson, L.T., Armbrust, E.V., Devol, A.H., Moffett, J.W., Stahl, D.A., Ingalls, A.E., 2015. Confounding effects of oxygen and temperature on the TEX86 signature of marine Thaumarchaeota. Proc. Natl. Acad. Sci. USA 112, 10979–10984. https://doi.org/10.1073/pnas.1501568112.

Robinson, S.A., Dickson, A.J., Pain, A., Jenkyns, H.C., O'Brien, C.L., Farnsworth, A., Lunt, D.J., 2019. Southern Hemisphere sea-surface temperatures during the Cenomanian-Turonian: implications for the termination of Oceanic Anoxic Event 2. Geology 47, 131–134. https://doi.org/10.1130/G45842.1.

Roeckner, E., Bäuml, G., Bonaventura, L., Brokopf, R., Esch, M., Giorgetta, M., Hagemann, S., Kirchner, I., Kornblueh, L., Manzini, E., Rhodin, A., Schlese, U., Schulzweida, U., Tompkins, A., 2003. The atmospheric general circulation model ECHAM 5. PART I: Model description. Max Planck Institute for Meteorology Report 349.

Ross, M.I., Scotese, C.R., 1988. A hierarchical tectonic model of the Gulf of Mexico and Caribbean region. Tectonophysics 155, 139–168. https://doi.org/10.1016/0040-1951(88)90263-6.

Roth, P., 1981. Mid-Cretaceous Calcareous Nannoplankton from the Central Pacific: Implications for Paleoceanography. Initial Reports of the Deep Sea Drilling Project, 62, vol. 75. U.S. Government Printing Office, pp. 471–489.

Schouten, S., Forster, A., Panoto, F.E., Sinninghe Damsté, J.S., 2007. Towards calibration of the TEX86 palaeothermometer for tropical sea surface temperatures in ancient greenhouse worlds. Org. Geochem. 38, 1537–1546. https://doi.org/10.1016/j.orggeochem.2007.05.014.

Schouten, S., Hopmans, E.C., Forster, A., van Breugel, Y., Kuypers, M.M., Sinninghe Damsté, J.S., 2003. Extremely high sea-surface temperatures at low latitudes during the middle Cretaceous as revealed by archaeal membrane lipids. Geology 31, 1069–1072. https://doi.org/10.1130/G19876.1.

Schouten, S., Hopmans, E.C., Schefuß, E., Sinninghe Damsté, J.S., 2002. Distributional variations in marine crenarchaeotal membrane lipids: a new tool for reconstructing ancient sea water temperatures? Earth Planet. Sci. Lett. 204, 265–274. https://doi.org/10.1016/S0012-821X(02)00979-2.

Schouten, S., Hopmans, E.C., Sinninghe Damsté, J.S., 2004. The effect of maturity and depositional redox conditions on archaeal tetraether lipid palaeothermometry. Org. Geochem. 35, 567–571. https://doi.org/10.1016/j.orggeochem.2004.01.012.

Sewall, J.O., van de Wal, R.S.W., van der Zwan, K., van Oosterhout, C., Dijkstra, H.A., Scotese, C.R., 2007. Climate model boundary conditions for four Cretaceous time slices. Clim. Past 3, 647–657. https://doi.org/10.5194/cpd-3-791-2007.

Sibuet, J.C., Ryan, W., 1979. Site 398: Evolution of the West Iberian Passive Continental Margin in the Framework of the Early Evolution of the North Atlantic Ocean. Initial Reports of the Deep Sea Drilling Project, 47 Pt. 2. U.S. Government Printing Office.

Sinninghe Damsté, J.S., Ossebaar, J., Schouten, S., Verschuren, D., 2012. Distribution of tetraether lipids in the 25-ka sedimentary record of Lake Challa: extracting reliable TEX86 and MBT/CBT palaeotemperatures from an equatorial African lake. Quat. Sci. Rev. 50, 43–54. https://doi.org/10.1016/j.quascirev.2012.07.001.

Taylor, K.W., Huber, M., Hollis, C.J., Hernandez-Sanchez, M.T., Pancost, R.D., 2013. Re-evaluating modern and Palaeogene GDGT distributions: implications for SST reconstructions. Glob. Planet. Change 108, 158–174. https://doi.org/10.1016/j.gloplacha.2013.06.011.

Tierney, J.E., Sinninghe Damsté, J.S., Pancost, R.D., Sluijs, A., Zachos, J.C., 2017. Eocene temperature gradients. Nat. Geosci. 10, 538–539. https://doi.org/10.1038/ngeo2997.

Tierney, J.E., Tingley, M.P., 2014. A Bayesian, spatially-varying calibration model for the TEX86 proxy. Geochim. Cosmochim. Acta 127, 83–106. https://doi.org/10.1016/j.gca.2013.11.026.

Tierney, J.E., Tingley, M.P., 2015. A TEX86 surface sediment database and extended Bayesian calibration. Sci. Data 2, 1–10. https://doi.org/10.1038/sdata.2015.29.

Topper, R.P., Trabucho Alexandre, J., Tuenter, E., Meijer, P.T., 2011. A regional ocean circulation model for the mid-Cretaceous North Atlantic Basin: implications for black shale formation. Clim. Past 7, 277–297. https://doi.org/10.5194/cp-7-277-2011.

Trabucho-Alexandre, J., Hay, W.W., De Boer, P.L., 2012. Phanerozoic environments of black shale deposition and the Wilson Cycle. Solid Earth 3, 29–42. https://doi.org/10.5194/se-3-29-2012.

Trommer, G., Siccha, M., van der Meer, M.T., Schouten, S., Sinninghe Damsté, J.S., Schulz, H., Hemleben, C., Kucera, M., 2009. Distribution of Crenarchaeota tetraether membrane lipids in surface sediments from the Red Sea. Org. Geochem. 40, 724–731. https://doi.org/10.1016/j.orggeochem.2009.03.001.

Villanueva, L., Schouten, S., Sinninghe Damsté, J.S., 2015. Depth-related distribution of a key gene of the tetraether lipid biosynthetic pathway in marine Thaumarchaeota. Environ. Microbiol. 17, 3527–3539. https://doi.org/10.1111/1462-2920.12508.

Wuchter, C., Schouten, S., Coolen, M.J.L., Sinninghe Damsté, J.S., 2004. Temperature-dependent variation in the distribution of tetraether membrane lipids of marine Crenarchaeota: implications for TEX86 paleothermometry. Paleoceanography 19, 1–10. https://doi.org/10.1029/2004PA001041.

Zhang, Y.G., Liu, X., 2018. Export depth of the TEX86 signal. Paleoceanogr. Paleoclimatol. 33, 666–671. https://doi.org/10.1029/2018PA003337.

Zhang, Y.G., Pagani, M., Wang, Z., 2016. Ring index: a new strategy to evaluate the integrity of TEX86 paleothermometry. Paleoceanography 31, 220–232. https://doi.org/10.1002/2015PA002848.

Zhang, Y.G., Zhang, C.L., Liu, X.L., Li, L., Hinrichs, K.U., Noakes, J.E., 2011. Methane index: a tetraether archaeal lipid biomarker indicator for detecting the instability of marine gas hydrates. Earth Planet. Sci. Lett. 307, 525–534. https://doi.org/10.1016/j.epsl.2011.05.031.